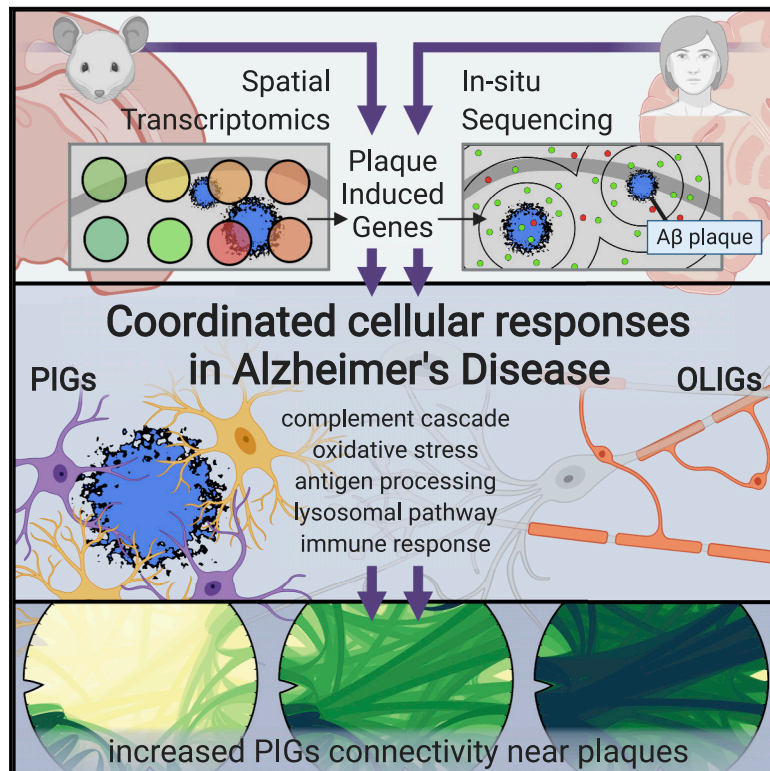


Spatial Transcriptomics and *In Situ* Sequencing to Study Alzheimer's Disease

Graphical Abstract



Authors

Wei-Ting Chen, Ashley Lu, Katleen Craessaerts, ..., Joakim Lundeberg, Mark Fiers, Bart De Strooper

Correspondence

mark.fiers@kuleuven.vib.be (M.F.), b.strooper@ukdri.ucl.ac.uk (B.D.S.)

In Brief

A combination of spatial transcriptomics and *in situ* sequencing on mouse and human brain demonstrates multicellular gene co-expression networks in Alzheimer's disease, two of which are induced by accumulating amyloid plaques. A plaque-induced gene (PIG) network mainly involving micro- and astroglia and an oligodendrocyte gene (OLIG) and myelination response are identified.

Highlights

- Spatial transcriptomics identifies a plaque-induced gene (PIG) network
- Spatial transcriptomics identifies an oligodendrocyte gene (OLIG) response in AD
- *In situ* sequencing in mouse and human confirms these responses at single-cell level
- PIG and OLIG responses are conserved over different neurodegenerative diseases



Resource

Spatial Transcriptomics and *In Situ* Sequencing to Study Alzheimer's Disease

Wei-Ting Chen,^{1,2,11} Ashley Lu,^{1,2,11} Katleen Craessaerts,^{1,2} Benjamin Pavie,^{1,2,3,4} Carlo Sala Frigerio,^{1,2,10} Nikky Corthout,^{1,2,3,4} Xiaoyan Qian,⁵ Jana Laláková,⁵ Malte Kühnemund,⁵ Iryna Voytyuk,^{1,2} Leen Wolfs,^{1,2} Renzo Mancuso,^{1,2} Evgenia Salta,^{1,2} Sriram Balusu,^{1,2} An Snellinx,^{1,2} Sebastian Munck,^{1,2,3,4} Aleksandra Jurek,⁶ Jose Fernandez Navarro,⁶ Takaomi C. Saido,⁷ Inge Huitinga,^{8,9} Joakim Lundeberg,⁶ Mark Fiers,^{1,2,10,*} and Bart De Strooper^{1,2,10,12,*}

¹VIB Center for Brain & Disease Research, Leuven 3000, Belgium

²KU Leuven, Department of Neurosciences, Leuven Brain Institute, Leuven 3000, Belgium

³VIB Bio Imaging Core, Gent 9052, Belgium

⁴VIB Bio Imaging Core, Leuven 3000, Belgium

⁵Cartana AB, Nobels väg 16, Solna 17165, Sweden

⁶Science for Life Laboratory, Department of Gene Technology, KTH Royal Institute of Technology, Solna, Stockholm 17121, Sweden

⁷Laboratory for Proteolytic Neuroscience, RIKEN Brain Science Institute, Wako-shi, Saitama 351-0198, Japan

⁸Department of Neuroimmunology, Netherlands Institute for Neuroscience, Royal Netherlands Academy of Arts and Sciences, Amsterdam 1105BA, the Netherlands

⁹Swammerdam Institute for Life Sciences, University of Amsterdam, Amsterdam 1098XH, the Netherlands

¹⁰UK Dementia Research Institute at University College London, London WC1E 6BT, UK

¹¹These authors contributed equally

¹²Lead Contact

*Correspondence: mark.fiers@kuleuven.vib.be (M.F.), b.strooper@ukdri.ucl.ac.uk (B.D.S.)

<https://doi.org/10.1016/j.cell.2020.06.038>

SUMMARY

Although complex inflammatory-like alterations are observed around the amyloid plaques of Alzheimer's disease (AD), little is known about the molecular changes and cellular interactions that characterize this response. We investigate here, in an AD mouse model, the transcriptional changes occurring in tissue domains in a 100- μ m diameter around amyloid plaques using spatial transcriptomics. We demonstrate early alterations in a gene co-expression network enriched for myelin and oligodendrocyte genes (OLIGs), whereas a multicellular gene co-expression network of plaque-induced genes (PIGs) involving the complement system, oxidative stress, lysosomes, and inflammation is prominent in the later phase of the disease. We confirm the majority of the observed alterations at the cellular level using *in situ* sequencing on mouse and human brain sections. Genome-wide spatial transcriptomics analysis provides an unprecedented approach to untangle the dysregulated cellular network in the vicinity of pathogenic hallmarks of AD and other brain diseases.

INTRODUCTION

Tremendous progress has been made to define cell states in physiological and pathological conditions using next-generation sequencing approaches. For example, in the Alzheimer's disease (AD) field, we know now that microglia display a stereotypical activated response to β -amyloid (A β) plaques (Keren-Shaul et al., 2017; Krasemann et al., 2017; Sala Frigerio et al., 2019; Sierksma et al., 2020). Neurons, astrocytes, and oligodendrocytes are more difficult to isolate than microglia, but single nuclei are a suitable alternative (Del-Aguila et al., 2019; Grubman et al., 2019; Mathys et al., 2019; Zhou et al., 2020). Cytoplasmic mRNA is less well presented in these samples (Lake et al., 2017; Thrupp et al., 2020), and the isolation methods induce artificial changes in expression profiles (van den Brink et al., 2017). A fundamental problem, however, is loss of most spatial information, including

the relationship of cells to amyloid plaques. Spatially barcoded arrays allow unbiased transcriptome profiling in tissue, maintaining the spatial localization of the sequenced molecules (Stahl et al., 2016; Rodrigues et al., 2019; Vickovic et al., 2019).

A central question in AD research is the relationship of amyloid plaques to the neurodegenerative process (Sevigny et al., 2016; Long and Holtzman, 2019; Schneider, 2020). Amyloid plaques might act as triggers or drivers of AD (Karran et al. 2011). Genetic analysis shows that risk of sporadic AD is associated with genes expressed in microglia that are responsive to amyloid deposition (Matarin et al., 2015; Keren-Shaul et al., 2017; Krasemann et al., 2017; Sala Frigerio et al., 2019; Salih et al., 2018; Jansen et al., 2019; Sierksma et al., 2020), but astrocytes, neurons, and oligodendrocytes also display altered molecular responses to amyloid plaques (De Strooper and Karran, 2016). The study of this "cellular phase of AD" should lead to a comprehensive



understanding of the complex interactions over time between those cells, which determine the pathogenic outcome triggered by A β deposition. Little is known, however, about the molecular changes occurring in cells in the vicinity of amyloid plaques.

Here we use spatial transcriptomics (ST) (Stahl et al., 2016) to measure, *in situ* in hundreds of small tissue domains (TDs), genome-wide transcriptomics changes induced by amyloid plaques. We complement this approach with an orthogonal *in situ* sequencing method (Qian et al., 2020) that visualizes hundreds of selected transcripts with cellular resolution. We integrated all of the information into a fully accessible database (<https://www.alzmap.org/>). In the current manuscript, we characterize two gene co-expression networks that appeared to be highly responsive to A β deposition. The 57 plaque-induced genes (PIGs) are a response over multiple cell types. PIGs become gradually co-expressed with increasing A β load in AppNL-G-F mice and encompass complement, endosomes and lysosomes, oxidation-reduction, and inflammation. A second network, oligodendrocyte genes (OLIGs), is enriched for genes involved in myelination and mainly expressed by oligodendrocytes. An OLIG is activated under mild amyloid stress but becomes depleted in microenvironments with high amyloid accumulation. Many PIGs and OLIGs show similar alterations in human brain samples, partially strengthening our observations.

RESULTS

We obtained three adjacent coronal sections (Figure 1A) by cryo-sectioning mouse brains from App^{NL-G-F} and C57BL/6 mice 3, 6, 12, and 18 months of age (Table S1; Figure S1A). The two outer sections were immunostained, whereas the middle one was processed for ST. Every coronal section contained more than 500 transcriptomics profiles of individual TDs, adding up to 10,327 transcriptomics profiles over 20 coronal sections. Each TD was annotated with spatial, pathological, and cellular information. We detected 31,283 \pm 7,441 unique molecular identifiers and 6,578 \pm 987 unique genes per TD (Figures S1B and S1C). We aligned each coronal section with 14 anatomical brain regions (Figure 1B) defined by the Allen Mouse Brain Atlas (Lein et al., 2006), and each TD was assigned to one of them (STAR Methods). The number of TDs varied between 112 (entorhinal cortex) and 2,114 (thalamus) (Figure 1B). We finally aligned the three sections to annotate each TD with A β load (6E10 staining), reactive astrocytes (GFAP), presence of neurons (NeuN), and nuclei (DAPI). All information is available on <https://www.alzmap.org/>.

ST in Adult Mouse Brains

The 10,327 transcriptomic profiles clustered according to brain regions using t-distributed stochastic neighbor embedding (t-SNE; Figure 1C). The transcriptomics profiles (Figures 1F and 1G) and landmark genes (Figures 1H and 1I) covering the somatic layers of the hippocampus segregated clearly into CA1, CA3, and DG subregions, demonstrating that ST is sufficiently powerful to identify precise anatomic regions in the brain. A good separation according to age and genotype was also observed (Figure 1D; see principal-component analysis on <https://www.alzmap.org/>). The spots of wild-type (WT) mice 12

and 18 months of age overlap (purple and red in Figure 1D), whereas the App^{NL-G-F} transcriptomics profile still changes between these two time points (yellow and green), in concordance with the progression of pathology over this period.

Linking Gene Expression Alterations to A β Accumulation

Amyloid deposition in App^{NL-G-F} mice starts around 3 months (Figure 2A). At 18 months, 1,565 \pm 167 plaques with surfaces of 78.5–4,950 μm^2 (i.e., a diameter of 10–80 μm) were detected per section. The diameter of a TD is 100 μm , and the thickness of a section is 10 μm (Figure 1A). Therefore, it is reasonable to assume that cells in the central section are exposed to amyloid plaques detected in the adjacent sections. We used the standard deviation of A β fluorescence intensity of pixels in a TD as the A β index (STAR Methods). This differentiates mild A β from intense A β accumulation (e.g., spot ID 474 from ID 466 in Figure 2B). In Figure 2C, we averaged the A β index of the TD per brain region, which shows consistency with A β immunostaining (Figure 2A), illustrating the progression of A β from the dorsal toward the ventral cortex, thalamus, and hippocampus. GFAP mRNA and protein indicating activated astroglia (Figure S2) are stable in physiological aging, with only a visible increase in the *stratum lacunosum moleculare* (CA_slm) of the hippocampus. In the aging App^{NL-G-F} model, GFAP staining spreads all over the brain, especially toward the cortical regions.

To understand changes in gene expression, we performed two differential expression analyses. The first compares App^{NL-G-F} with C57BL/6 mice (genotype model), the second investigates the effect of A β accumulation on gene expression (A β model). We validated the A β model using a classic RNAscope experiment (Figures 2D and 2E) of six transcripts that, according to the model, were significantly dysregulated in App^{NL-G-F} mice at 18 months of age: *Cst7* (log fold change [LFC], 1.91), *Cd68* (LFC, 1.70), *Ct1qa* (LFC, 1.04), *Slc1a3* (LFC, 0.57), *Clu* (LFC, 0.41), and *Mbp* (LFC, -0.37). We grouped the cells in 5 concentric rings around the amyloid plaques (STAR Methods). We measured the mean intensity of hybridization per cell in amyloid plaque cellular niches (ring 1, cells within 10 μm of A β -positive areas) compared with tissue far from plaques (ring 5, the most distant ring is 195 pixels or 54.6 μm away from ring 1). As shown in Figure 2D, the ST data highly correlate with the RNAscope data (Pearson correlation = 0.92, $p = 0.009$), providing confidence in the approach.

We compared both models by plotting LFC by genotype (the genotype axis) against LFC by A β accumulation (the A β axis) per time point. This provides information regarding gene expression alterations according to genotype, A β exposure, and age. We employed GOrilla (Eden et al., 2009) on genes ranked according to LFC along the genotype axis and along the A β axis and identified 13 functional supercategories (Figure S3A; Table S2). Antigen processing, chemotaxis, lysosomal degradation, and inflammation are upregulated along the A β and genotype axes at 18 months. Interestingly, we find a clear switch of direction of the myelin category, which is up at 3 and down at 18 months along the A β but not the genotype axis.

Genes with similar expression patterns (co-expression) are likely to have similar functions and can be grouped into

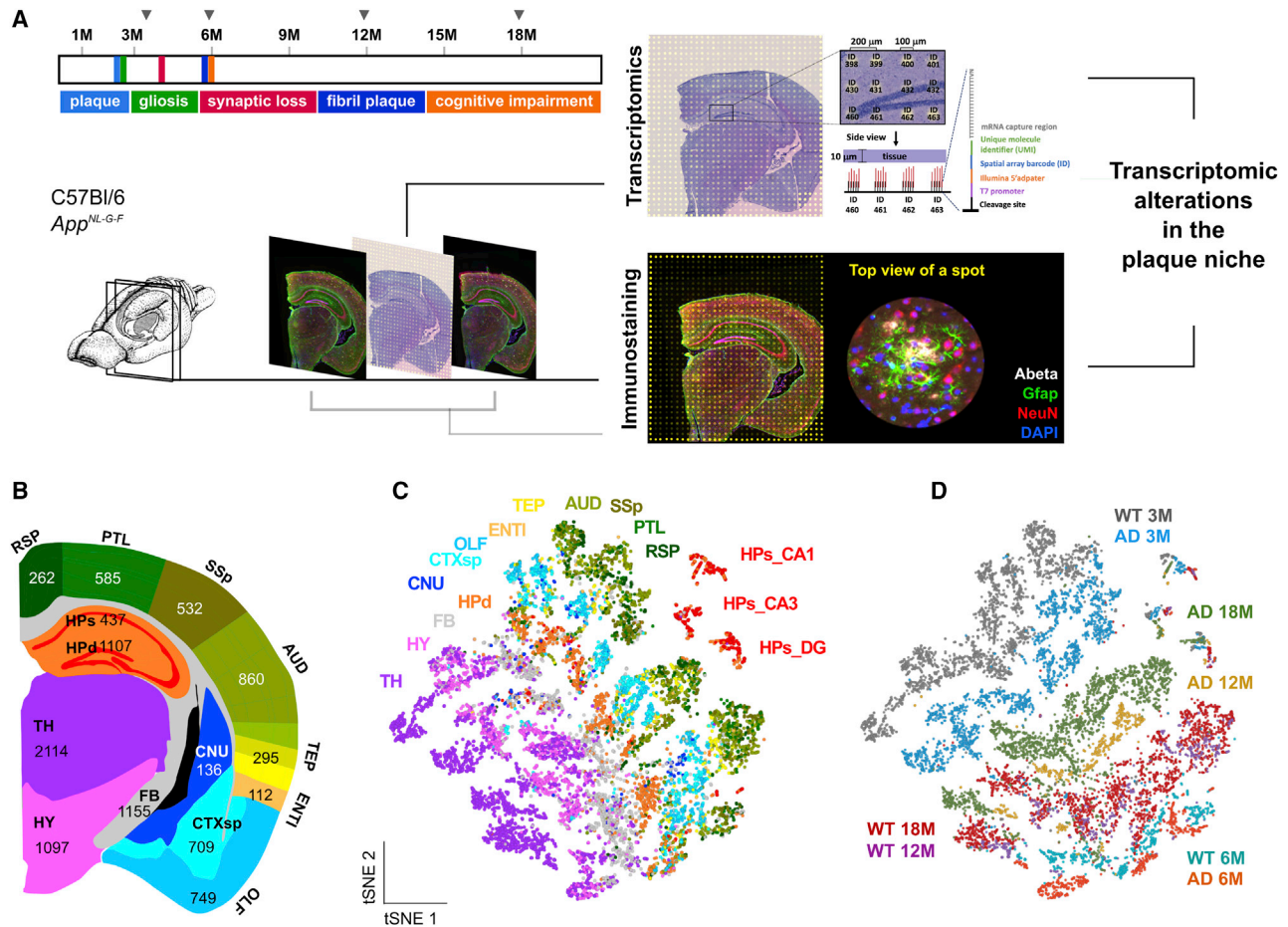


Figure 1. Spatially Resolved Transcriptomics Profiles in Adult Mouse Brain

(A) Sequential 10- μ m coronal sections of *App^{NL-G-F}* and WT brains were collected at 3, 6, 12, and 18 months of age. The middle section was used for ST and the two adjacent sections for immunostaining.

(B) Total number of TDs per brain region.

(C and D) t-SNE plots of the 10,327 transcriptomics profiles. TDs were colored according to brain region (C) or genotype and age (D). TH, thalamus; HYP, hypothalamus; FB, fiber tract; HPd, dendritic layer of the hippocampus; HPs, somatic layer of the hippocampus; CNU, cerebral nucleus; CTXsp, cortical subplate; OLF, olfactory area; ENT1, entorhinal area; TEP, temporal association area, ectorhinal area, and perirhinal area; AUD, auditory area; SSp, primary somatosensory area; PTL, posterior parietal association area; RSP, retrosplenial area.

See also Figure S1.

modules by weighted gene co-expression network analysis (WGCNA) (Zhang and Horvath, 2005). We investigated the 50% most variable genes across the full library of 10,327 ST transcriptome profiles and identified 12 modules (Table S3; Figure S3B), for which we extracted the hypothetical biological functions by GOrilla (Table S4), the expression alteration to A β exposure and to genotype at 3 and 18 months (Figure S3B), the cellular signature (Figures S3C–S3E), and the affected brain regions (<https://www.alzmap.org/> regional plot; STAR Methods). We focus here on the purple and red WGCNA modules that were most responsive to A β (Figure S3B). Agreeing with the ontology analysis above, the red module largely represents the functional myelin category, which goes up in the early and down in the late stage along the A β axis, whereas the purple module represents the chemotaxis, lysosomal

degradation, inflammation, and especially antigen processing categories, which do not react in the early stage but become significantly upregulated in the disease and A β axes in the late stage.

Identification of the PIG Module

The purple WGCNA module, which we call “plaque-induced genes” (PIGs), is the most reactive one along the A β as well as the genotype axis at 18 months of age (Figure S3B). This module, which contains 57 genes, is initially slightly up-regulated (Figure 3A) but increases sharply between 6 and 12 months to stabilize as a homogeneous response over the whole brain (Figure 3B). We identify a moderate but significant correlation between A β accumulation and PIG expression among all TDs in *App^{NL-G-F}* mice at 18 months (Pearson correlation = 0.39,

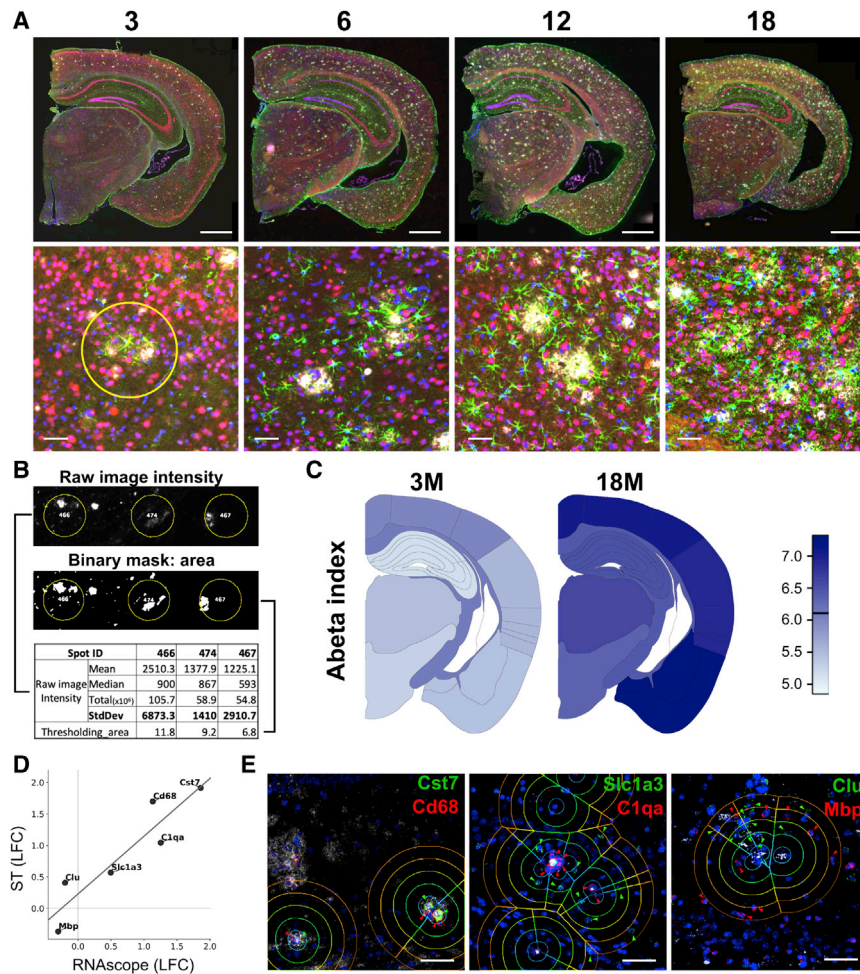


Figure 2. Linking Gene Expression Alterations to A β Load

(A) Immunostaining of A β (6E10, white), astrocytes (GFAP, green), neurons (NeuN, red), and nuclei (DAPI, blue) at the indicated ages (months). Scale bars, 500 μ m. Bottom: magnification of TDs (yellow circle, 100 μ m in diameter) in the primary somatosensory area of the cortex. Scale bars, 25 μ m.

(B) Quantification of A β load. Yellow circles indicate the associated TDs. Standard deviation of pixel intensities has the best correlation with independent expert analysis and is used as the A β index of a TD.

(C) The mean of the log-transformed A β index per brain region is plotted at the indicated ages.

(D) Scatterplot showing the LFC as a function of A β exposure of each target as detected via ST (y axis) or RNAscope (x axis), which is shown in (E) (targets: red or green, arrowheads) with 5 concentric rings of plaques. Pearson correlation = 0.92, $p = 0.009$. Scale bars, 50 μ m.

See also [Figure S2](#).

ARM microglia genes ([Figure 3D](#)). Thirty-six PIGs were not defined previously as disease-associated glia genes. Activated microglia and astrocytes contribute to the top 10 most connected hub genes (red in [Figure 3D](#); *Ctsd*, *C4b*, *Cst3*, *Apoe*, *C4a*, *Gfap*, *Tyrobp*, *Lyz2*, *Trem2*, and *B2m*). We evaluated whether the PIGs could be identified in a human dataset ([Mathys et al., 2019](#)). Among the 41 cellular subpopulations ([Mathys et al., 2019](#)), the highest association of PIGs is with an AD-associated microglial signature (*Mic1*; odds ratio, 4.28; [Figure S3E](#)). We

$p = 0$) ([Figure 3C](#)), indicating that PIG expression increases gradually with accumulating A β over all brain regions.

Based on the ontology analysis ([Table S4](#)), we conclude that the module is involved in activation of the classic complement cascade (gene ontology [GO]: 0006956; i.e., *C1qa*, *C1qb*, *C1qc*, *C4a*, and *C4b*), but also in effector mechanisms triggered by the complement cascade ([Schmidt and Gessner, 2005](#); [Thielens et al., 2017](#)), such as endocytosis (GO: 0045807; i.e., *Fcer1g*, *Fcgr3*, *B2m*, *Cd63*, *Cyba*, *Apoe*, *Clu*, and *Axl*), lysosomal degradation (GO: 0005764; i.e., *Hexa*, *Hexb*, *Ctsa*, *Ctsb*, *Ctsd*, *Ctsh*, *Ctsl*, *Ctss*, *Ctsz*, *Laptm5*, *Man2b1*, *Cd63*, *Gusb*, *Lgmn*, *Npc2*, *Grn*, *Gns*, *Prdx6*, and *Cst3*), antigen processing and presentation (GO: 0002474; i.e., *Fcer1g*, *Fcgr3*, *B2m*, *H2-D1*, and *H2-K1*), immune response (GO: 0002376; i.e., *Csf1r*, *Cx3cr1*, *Ly86*, *Trem2*, *Tyrobp*, and *Vsir*), and oxidation-reduction processes (GO: 0055114; i.e., *Cyba*, *Prdx6*, and *Gpx4*).

We investigated the cellular signatures of the PIG module and identified strong associations with activated microglia (disease-associated microglia [DAM]) or activated response microglia [ARM]; odds ratio, 3.71 ([Keren-Shaul et al., 2017](#); [Sala Frigerio et al., 2019](#)) and inflammatory astrocytes (A1; odds ratio, 3.84) ([Zamanian et al., 2012](#); [Figure S3D](#)). We highlight 5 PIGs that overlap with A1 astrocyte markers and 18 PIGs that are DAM/

highlight the gene expression alterations of the mouse orthologs of the human *Mic1* marker genes ([Figures 3E and 3F](#), orange and green) in function of A β exposure or genotype. The analysis in mice shows that the *Mic1* response in the human brain is part of a larger multicellular coordinated response toward amyloid plaques and that this response evolves over time.

In Situ Sequencing Provides Cellular Resolution to the PIG Module

ST suggested a multicellular response around amyloid plaques, but we sought to confirm this using an orthogonal, independent approach that provides single-cell resolution. We applied *in situ* sequencing (ISS), which identifies *in situ* barcodes of many target-specific probes in one go ([Qian et al., 2020](#)). We used customized probes to map the expression of PIGs together with cell type markers (*Itgam*, *Cx3cr1*, and *Csf1r* for microglia; *Slc1a3*, *Gfap*, and *Clu* for astrocytes; *Syp* for neurons; and *Plp1* for oligodendrocytes; [Figures 4A–4C](#)). We generated two ISS libraries of *App*^{NL-G-F} and two of WT mice at 18 months of age. We quantified gene expression as the number of fluorescent puncta per gene and grouped the puncta in 5 concentric rings around the amyloid plaques ([Figure 4D](#)). Among the 54 detected PIGs, 51 PIGs are significantly enriched in ring 1 (log₂

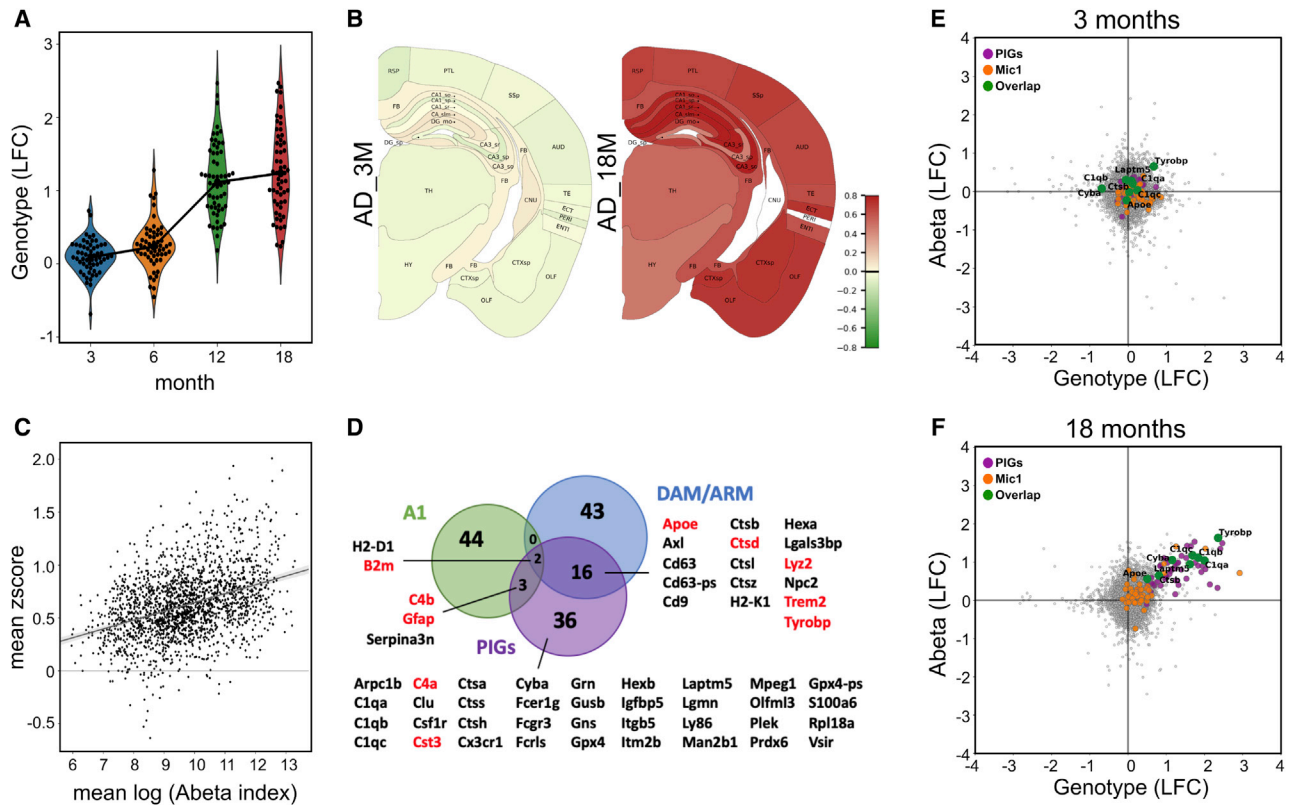


Figure 3. Identification of Aβ plaque-induced genes (PIGs)

The PIG module is the WGCNA module with the largest change in function of Aβ exposure at 18 months (see text and Figure S3B).

(A) LFCs of 57 PIGs in the genotype model at the indicated age. Each dot represents a PIG.

(B) Average of the mean Z score of PIGs per region in *App^{NL-G-F}* mice.

(C) The mean Z score of 57 PIGs in each TD (y axis) is positively correlated with the mean of the log-transformed Aβ index (x axis). Pearson correlation = 0.39, $p = 0$.

(D) Venn diagram highlighting the overlap of PIGs with ARM/DAM microglia and A1 astrocytes. See also Figure S3D. The top 10 connected hub genes are highlighted in red.

(E and F) Scatterplots at 3 (E) and 18 (F) months of age. The y axis represents the LFC of gene expression in the TDs in function of log-transformed Aβ index. The x axis represents the LFC of gene expression in *App^{NL-G-F}* versus WT mice. Individual genes of the PIG module (purple), mouse orthologs of human AD-associated microglia markers (Mic1, orange; Mathys et al., 2019), and overlaps between the two datasets (green) are indicated.

See also Figure S3E.

odds ratio [L_2OR] > 0, $padj < 0.05$), whereas *C1qb* is significantly depleted in ring 1 ($L_2OR < 0$, $padj < 0.05$; Figure 4E). The results from ISS (L_2OR of gene expression in ring 1 compared with puncta in rings 1–5) correlate well with the results from ST (LFC of gene expression in the Aβ model; Figure 4E; correlation = 0.68, $p = 3.04e-09$).

To investigate the cellular signature of the PIG network, we developed an approach that assigns each punctum to a cell type by calculating the enrichment of cell type marker puncta within its 5-μm radius, not including the punctum under investigation (STAR Methods). We tested the method by predicting the cell identity of each marker gene (Figure 4G). It is clear that the PIG response to Aβ is largely contributed by microglia and, to a lesser extent, astroglia (Figure 4H). Some PIGs are, however, significantly enriched in multiple cell types. For example, *Cyba* is expressed in microglia but also in oligodendrocytes, and *Cd9* is expressed in astrocytes, microglia, and oligodendrocytes. Some

inflammatory molecules (*H2-K1*, *Ly86*, and *Mpeg1*) and lysosomal enzymes (*Lgmn* and *Ctsa*) are expressed by microglia but also by neurons. In addition, we find enrichment of regulators of lysosomal degradation (*Gns* and *Grn*), an inhibitor of Aβ aggregation (*Itm2b*), and a regulator of insulin growth factor (*Igfbp5*) expressed in neurons. In *App^{NL-G-F}* mice, most PIGs are enriched in the same cell types as in WT mice, whereas some genes become expressed in microglia (e.g., *C1qa*, *Gusb*, *Hexa*, *Lgals3bp*, and *Plek*) or in astrocytes (e.g., *Gns*, *Gpx4*, and *Itgb5*). In addition, *Serpina3* switches major site of expression from neurons to astrocytes, whereas *C4a/C4b* is expressed in astrocytes and also becomes expressed in oligodendrocytes in *App^{NL-G-F}* mice. Although we have less statistical power to investigate PIGs in the plaque cellular niches (ring 1), for many we can confirm their cellular expression (Figure 4H). Interestingly, *Cts/* and *Apoe* become expressed in microglia only in the amyloid plaque niche.

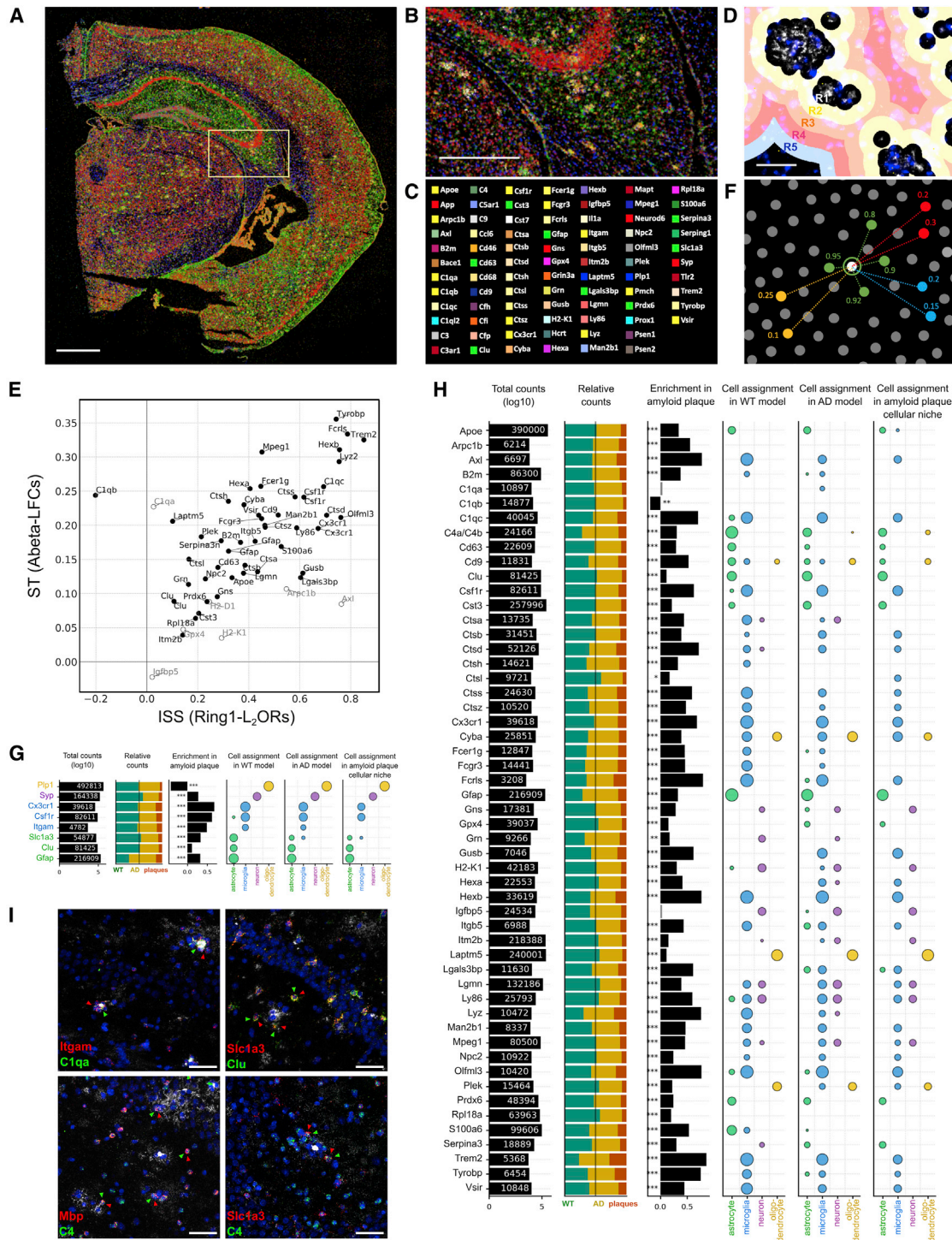


Figure 4. Cellular Signature of PIGs Identified by ISS

(A and B) Distribution of 84 genes (PIGs and cell type marker genes) in the coronal section (A) and magnification of the hippocampus (B) of *App^{NL-G-F}* mice at 18 months of age, demonstrated by *in situ* sequencing (ISS).

(C) Color of 84 genes displayed in (A) and (B), including red neuronal (i.e., *Syp*, *Neurod6*, and *Grin3a*), yellow microglial (i.e., *Ilgam*, *Cx3cr1*, and *Csf1r*), green astroglial (i.e., *Slc1a3*, *Gfap*, and *Serpina3n*), and blue oligodendroglial transcripts (i.e., *Pip1* and *Laptm5*).

(D) Areas circumscribing amyloid plaques from R1 (ring 1, the closest area) to R5 (ring 5, the most distant area). Amyloid plaques (6E10) are white, whereas nuclei (DAPI) are blue.

Scale bars, 800 μ m (A), 400 μ m (B), and 50 μ m (D).

(legend continued on next page)

Finally, we validated the expression of complement components (*C1qa*, *C4*, and *Clu*) using RNAscope *in situ* hybridization in *App^{NL-G-F}* mice at 18 months of age. We confirm that *C1qa* was expressed by *Itgam*-positive cells (microglia), *Clu* by *Slc1a3*-positive cells (astrocytes), and *C4* by *Mbp*-positive cells (oligodendrocytes)—all close to amyloid plaques (Figures S4I and S4B). The cellular signature of these 3 complement components, as examined by RNAscope, is consistent with the ISS analysis.

Co-expression of Micro- and Astroglia Genes in the PIG Module

We wondered to what extent the correlation in expression between PIGs in different cells was driven by accumulating A β pathology. We performed WGCNA on only the PIGs, separating all ST TDs into WT and four quantiles of AD according to A β index (Figure 5). WGCNA yields a connectivity matrix indicating how strongly changes in the expression of each gene correlate with changes in the expression of all other genes. The results are visualized by the Circos plots in Figure 5, which demonstrate how the network gradually builds up with increasing A β exposure.

In WT mice, the overall connectivity of the PIGs is relatively low, and the PIGs are split into 3 clusters (Figure 5; green, blue, and orange). The ISS (Figure 4H) demonstrates an enrichment of astroglia-expressed genes (7 of 12) in the green cluster, whereas the blue (14 of 23) and orange (14 of 18) clusters are enriched with PIGs expressed in microglia. In the WT situation, the orange PIGs are not or hardly interconnected. They become recruited in the PIGs when exposed to increasing amounts of A β in *App^{NL-G-F}* mice. The connectivity between the PIGs strengthens within and over the three clusters as a function of increasing A β index. In Q4 (lowest amyloid load), co-expression remains weak overall. In Q3, several pairs of genes in the blue and orange clusters become strongly co-expressed; for instance, the cell-cell adhesion/mobility molecules *Lgals3bp* and *Cx3cr1*, the glycosidases *Lyz2* and *Gusb*, and a calcium/zinc binding protein, *S100a6*. In Q2 and even more in Q1, a strong connection is established between the three clusters. The strongest connections are between *Ctsd* (green) and *C1qa*, *C1qb*, *Ctsb*, *Ctss*, and *Hexb* (blue) or between *Apoe* (green) and *C1qb* (blue). The strongest connections between the orange and the other 2 clusters go from *Trem2* and *Tyrbp* (orange) to *Ctsd*, *B2m*, and *Apoe* (green) and to *C1qa*, *C1qb*, *Hexb*, and *Ctss* (blue). Although the increased connection of *Apoe* (in a control situation exclusively expressed in astroglia) with microglia genes in the context of amyloid plaques is explained at least partially by induction of

expression of *Apoe* in microglia close to plaques (Figure 4H), most of the other PIGs remain expressed in their respective cell types, and the increasing interaction indicates co-expression of genes across different cell types.

An Oligodendrocyte Module Displays Diverse Regional Responses

The second most altered module, red, in the WGCNA (Figure S3B) is composed of 165 genes (Table S3) that are mainly expressed by oligodendrocytes, hence the name “OLIG module.” The most enriched functional classes of this module are GO: 0007272 ensheathment of neuron, GO: 0043209 myelin sheath, GO: 0008366 axon ensheathment, and GO: 0042552 myelination (Table S4). The top 10 hub genes of the OLIG module are myelin-related transcripts: *Pip1*, *Mbp*, *Mobp*, *Cldn11*, *Mal*, *Apod*, *Cnp*, *Trf*, *Fth1*, and *Plekhh1*. Comparing OLIG with published mouse single-cell databases confirms a strong association with oligodendrocytes (odds ratio, 4.76; Figure S3C) and a mild association with activated microglia (DAM/ARM; odds ratio, 1.40; Figure S3D). OLIG associates strongly (odds ratio, 4.06) with the human AD-associated oligodendrocytes Oli0 (Mathys et al., 2019; Figure S3E). We highlight 20 mouse orthologs of human Oli0 markers (Figures 6A and 6B, orange and green). Several Oli0 orthologs are up- or downregulated together with the OLIG module.

Similar to the myelin category (Figure S3A), the OLIG module is globally upregulated along the genotype axis in *App^{NL-G-F}* compared with WT mice at 3 and 18 months (see genotype LFCs in Figures 6A and 6B) and across the brain (Figure S5A). This genotype effect might reflect an overall response of the mouse brain to the humanized and mutated *App* gene. However, when we isolate the effect of A β exposure (A β axis) from the genotype, an interesting alteration of the expression of the OLIG module is observed: a global positive correlation at 3 months and a negative one at 18 months (Figures 6A and 6B). There is also clear variation in this response over different brain areas (Figure 6C). Comparing the amyloid profiles in Figure 2C with the OLIG expression profiles in Figure S5C, it becomes clear that the main driver of OLIG expression is not the A β index but the brain region itself (Figure 6C). At 3 months of age, we identified a significantly positive OLIG-A β correlation in fiber tract (FB), thalamus (TH), and hypothalamus (HY), whereas a significantly negative OLIG-A β correlation is seen in the entorhinal cortex (ENTI) and several layers of the hippocampus. At 18 months, we identified a significantly negative OLIG-A β correlation in auditory areas (AUDs), whereas significantly positive OLIG-A β correlations are seen in the ENTI and hippocampus (padj < 0.0001).

(E) Scatterplot comparing gene expression alterations as a function of A β exposure between ST and ISS in *App^{NL-G-F}* mice at 18 months of age. The y axis shows the LFC of each target according to the log-transformed A β index as detected via ST. The x axis shows the enrichment (log₂ odds ratio [L₂OR]) of each target in ring 1 (the plaques), as detected via ISS. Black spots are significant, whereas gray are not significant.

(F) Example of distance scores between a single punctum of interest (white) to cell type markers in a 5- μ m radius. See also Figure S7.

(G and H) Cellular signatures of the selected markers (G) and PIGs (H). Total counts, total number of puncta of each gene detected across 4 coronal sections from 2 genotypes; relative counts, the proportion of puncta detected in WT and *App^{NL-G-F}* mice and in plaques in *App^{NL-G-F}* mice, respectively; enrichment in amyloid plaques, L₂OR of gene puncta in plaques using a binominal test, with a negative value indicating depletion; cell assignment, enrichment of each gene in a particular cell type (Benjamini-Hochberg-corrected $p < 0.05$). The size of the balls is proportional to L₂OR.

(I) Cellular signatures of *C1qa*, *Clu*, and *C4* validated by RNAscope in *App^{NL-G-F}* mice at 18 months (microglia, *Itgam*; astroglia, *Slc1a3*; oligodendroglia, *Mbp*). *C1qa* is colocalized with *Itgam*, *Clu* is colocalized with *Slc1a3*, and *C4* is colocalized with *Slc1a3* or *Mbp*. Amyloid plaques, white; nuclei (DAPI), blue. Scale bars, 50 μ m.

See also Figure S4.

	Q1	Q2	Q3	Q4	
Number of tissue domain	3M	179	338	613	855
	6M	69	57	93	259
	12M	204	150	107	27
	18M	793	699	431	104
	Total	1245	1244	1244	1245
	mean of log (Aβ index)	7.70	6.50	5.57	4.73

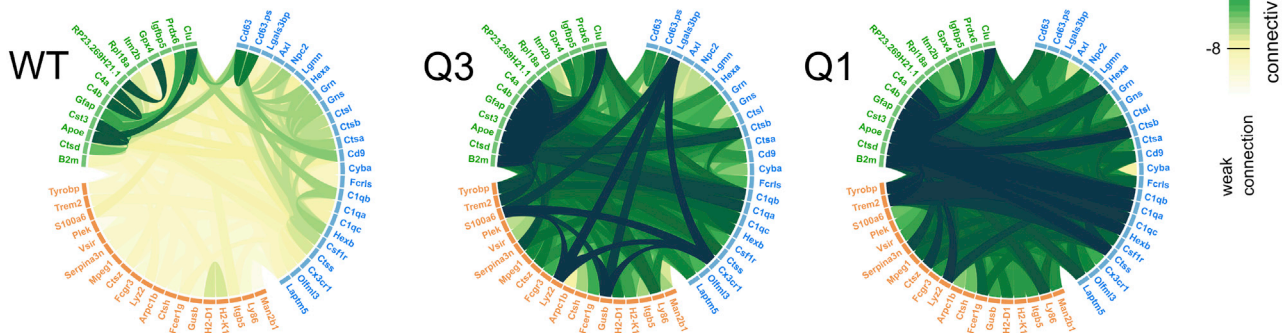


Figure 5. Gradual Co-expression of PIGs According to A β Accumulation

For a Figure360 author presentation of Figure, see <https://doi.org/10.1016/j.cell.2020.06.038>

The table shows the number of TDs of *App*^{NL-G-F} mice per age per quantile and the level of A β accumulation. The green lines in the Circos plots indicate the strength of the connectivity score between gene pairs. Segregation into 3 clusters (blue, green, and orange) is based on the WGCNA analysis in the WT. Note the dose-sensitive increase in connection of genes with increasing A β accumulation from Q4 to Q1, hence the name PIGs.

We thus analyzed in more detail the relationship between A β index and OLIG expression as a function of these regional differences. As shown in Figure 2, A β deposition varies from region to region over disease progression. Thus, even at 3 months, there are TDs exposed to high A β (i.e., 179 TDs in Q1; Figure 5). OLIG expression at 3 months increases with mild A β accumulation in TDs distributed over Q4–Q2 (Figure 6D). However, expression of OLIG exhibits a trend toward decreasing in the TDs, with the highest A β exposure at 3 months (Q1, which has 21 times more A β than Q4). In addition, the sum of connectivity strength of gene pairs of the OLIG module is strongest in TDs with low A β exposure (Q4; Figure S5B). To further confirm the findings, we performed a limited series of RNAscope experiments using probes against 4 OLIGs (*Plp1*, *Mbp*, *Olig2*, and *Cnp*) in *App*^{NL-G-F} mice at 3 months of age over whole coronal brain sections (Figures 6E, 6F, S5D, and S5E). The results show that the 4 OLIGs are significantly depleted around dense amyloid plaques even at 3 months. We suggest that the OLIG module is highly expressed and connected under mild A β exposure but decreased in microenvironments with dense A β accumulation. Thus, part of the regional variation in the OLIG module is linked to differential A β exposure.

Visualization of the PIG and OLIG Modules in Human Brains

Post-mortem human brain samples were obtained from three AD patients and three non-demented control subjects. The selected AD brains were advanced in disease with amyloid stage C (Thal

et al., 2002) and neurofibrillary tangle stage V–VI (Braak and Braak, 1991; Table S5; Figure S6A). The RNA quality of the 6 samples was good (RNA integrity number [RIN]), 8.4 ± 0.8 ; Table S5). We profiled tissue from the superior frontal gyrus (Brodmann area 10), which is of relevance to AD (Valdés Hernández et al., 2018). We report a total of 222 gene expression profiles, including 45 human orthologs of PIGs, 42 human orthologs of plaque-reactive genes in the OLIG module, and a series of cell type markers (Table S6). As shown in Figures 7A and S6B, the cellular markers provide a good overview of the cellular distribution in this brain area. The PIG module (Figure 7B, purple) and the OLIG module (Figure 7C, red) genes are enriched, respectively, in the gray and white matter, as expected. Cell type markers show reliable prediction of cell identity (*GRIP1*, *PPFIA2*, *KCNIP4*, *PTK2B*, and *DLGAP1* for neurons; *BLNK*, *C1QA*, *FCGR2A*, *CX3CR1*, *LAPTM5*, *TMEM119*, *HLA-DRA*, and *C1QC* for microglia; *MAL*, *ERMN*, *MOBP*, and *PLP1* for mature oligodendrocytes; *ALDH1L1*, *ADGRV1*, *CLU*, *SLC1A2*, *AQP4*, and *GFAP* for astrocytes; Figure S6C; Table S6).

We investigated the distribution of the human orthologs of the PIGs in control and AD brains using the same methodology as used above to analyze ISS data in mice. Most PIGs are expressed in the same cell types in AD and controls. Also in human, the 3 submodules of the PIG module are expressed by astrocytes (green cluster) and microglia (blue and orange clusters) in controls (Figure 7D). However, we also identify 9 PIGs enriched in neurons (*LGDN*, *HEXB*, *HEXA*, *CTSB*, *CTSA*, *GNS*, *GPX4*, *CTSD*, and *ITM2B*), whereas 2 PIGs are enriched in

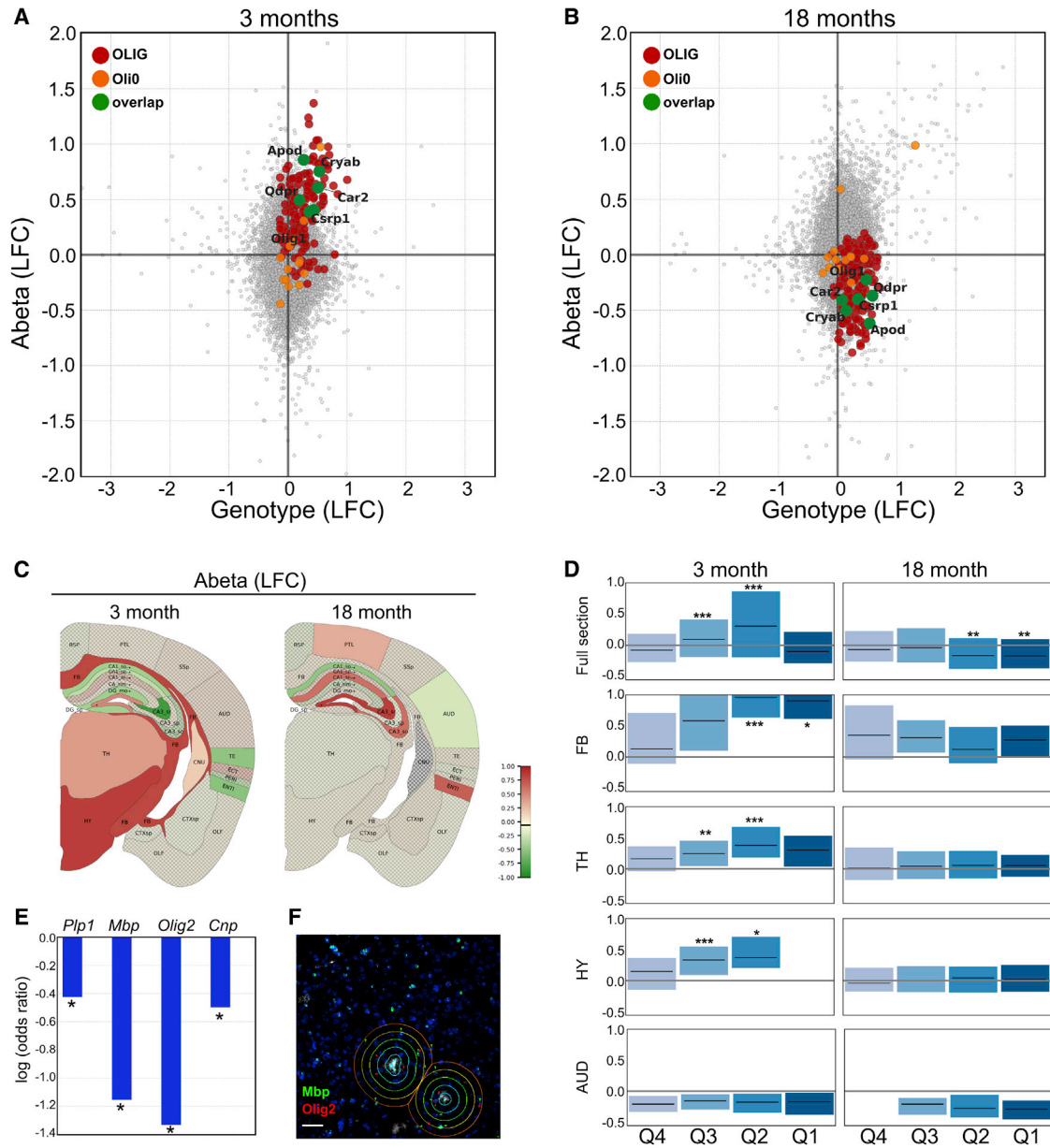


Figure 6. Spatial and Temporal Response of the OLIG Module to A β Accumulation

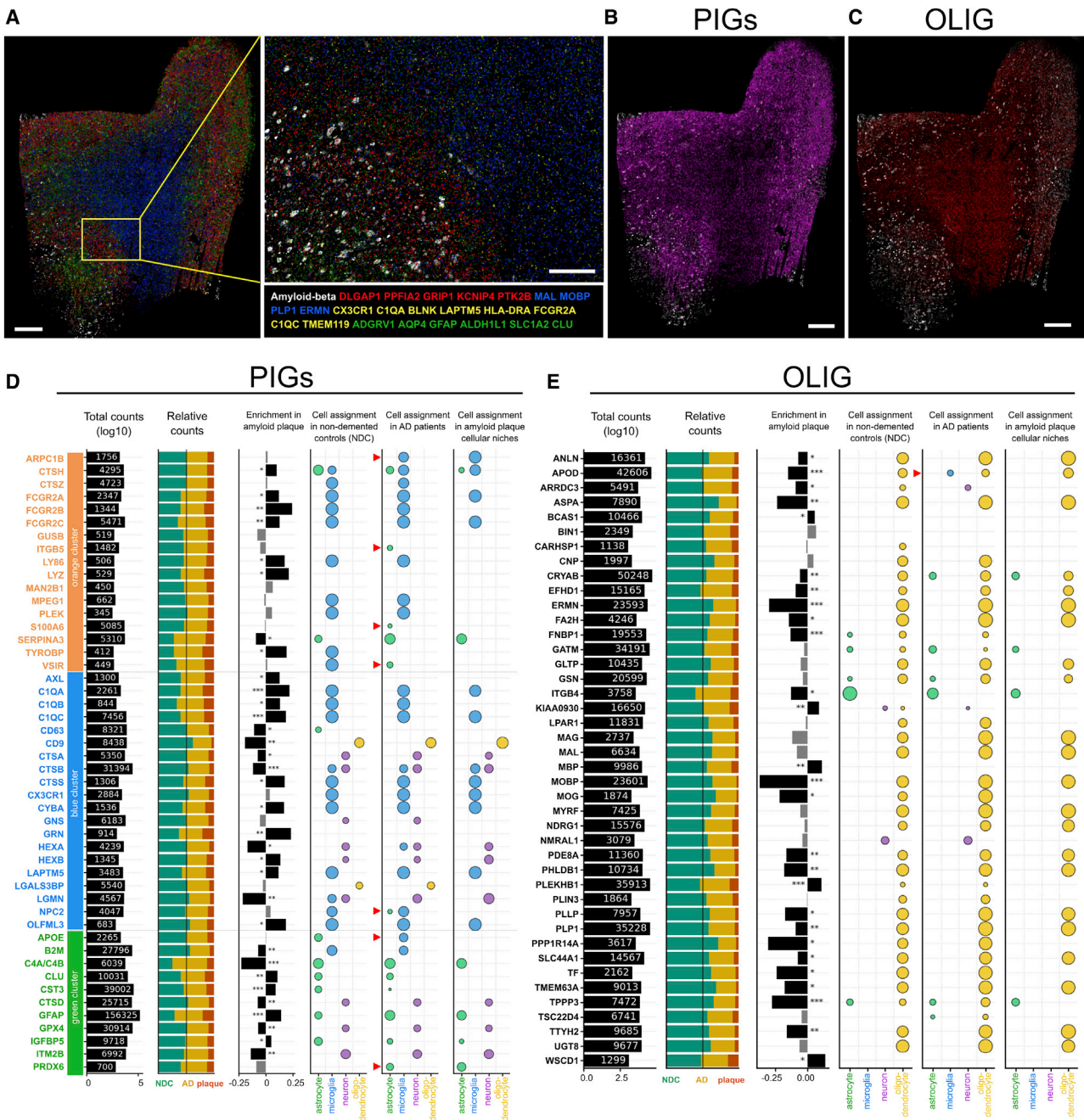
(A and B) Scatterplots at 3 (A) and 18 (B) months of age. The y axis represents LFC of gene expression in TDs as a function of log-transformed A β index. The x axis represents LFC of gene expression in *App*^{NL-G-F} versus WT mice. Individual genes of the OLIG module (red spots), mouse orthologs of human AD-associated oligodendrocyte markers (Oli0, orange spots; Mathys et al., 2019), and overlaps between the two datasets (green spots) are indicated. See also Figure S3B. (C) Average of LFCs of 165 OLIG genes as a function of log-transformed A β index per region per age in *App*^{NL-G-F} mice at 3 and 18 months (mesh, non-significant LFC, $p > 0.0001$).

(D) OLIG expression in subsets of TDs according to A β exposure. The y axis represents expression of OLIG (average Z score normalized to the mean of the lowest A β quantile set, Q4, at the full-brain level). * $p < 0.05$, ** $p < 0.005$, *** $p < 0.0005$, Mann-Whitney U test compared with Q4, p values corrected by Benjamini-Hochberg procedure.

(E) Quantification of (F).

(F) Combined RNAscope and immunofluorescence analysis of *Mbp*, *Olig2*, *Plp1*, and *Cnp* in the vicinity of amyloid plaques (6E10, white) in *App*^{NL-G-F} mice at 3 months of age. Nuclei are blue (DAPI). Scale bar, 50 μ m.

See also Figure S5.



oligodendrocytes (*LGALS3BP* and *CD9*). *PLEK*, *CYBA*, and *LAPTM5* are significantly enriched in oligodendrocytes in mice but significantly enriched in microglia in humans. We eventually

could confirm only 18 of the 45 detectable PIGs as significantly enriched in amyloid plaque cellular niches, including 9 microglial PIGs (i.e., *C1QA*, *C1QB*, *C1QC*, *TYROBP*, *LY86*, *CYBA*, *FCGR2*,

OLFML3, and *LAPTM5*), 5 astroglial PIGs (i.e., *GFAP*, *CLU*, *CTSH*, *CST3*, and *IGFBP5*), and 5 PIGs expressed in multiple cell types (*CTSH*, *GRN*, *LYZ*, *HEXB*, and *AXL*; $L_2OR > 0$, $padj < 0.05$). Interestingly, we found significant expression of *APOE* and *ARPC1B* in microglia and significant expression of *NPC2*, *S100A6*, *ITGB5*, *PRDX6*, and *VSIR* in astrocytes in AD patients but not in controls, indicating disease-related glial activation in AD patients.

We analyzed, in a similar way, the cellular signature of 42 human orthologs selected from the top rank of differentially expressed genes of the OLIG module (Figure 7E). Twenty-two genes are significantly depleted in the amyloid plaque cellular niches (*CRYAB*, *ANLN*, *SLC44A1*, *PLP1*, *ARRDC3*, *EFHD1*, *ITGB4*, *FNBP1*, *FA2H*, *APOD*, *TTYH2*, *PDE8A*, *PLLP*, *TMEM63A*, *PHLDB1*, *MOG*, *ASPA*, *TF*, *TPPP3*, *ERMN*, *PPP1R14A*, and *MOBP*; $L_2OR < 0$, $padj < 0.05$). Five genes are significantly higher expressed in the amyloid plaque cellular niches (*WSCD1*, *MBP*, *PLEKHB1*, *KIAA0930*, and *BCAS1*; $L_2OR > 0$, $padj < 0.05$). Most of the human orthologs in the OLIG module are significantly enriched in oligodendrocytes in control and AD patients, except for enrichment of *KIAA0930* and a redox sensor (*NMRAL1*) in neurons and enrichment of regulators of protein aggregation (*CRYAB* and *GSM*), cell mobility/adhesion molecules (*TPPP3* and *ITGB4*), and a catalyzer of creatine (*GATM*) in astrocytes. Interestingly, *APOD*, a lipoprotein-encoding gene mostly expressed in the brain and upregulated in AD (Bhatia et al., 2019) that is normally expressed by oligodendrocytes, also becomes significantly enriched in microglia in AD patients but not in control subjects.

When comparing these data with the results from the mouse experiments, one should take into account the species differences but also the fact that, in the mouse, only amyloid plaque-induced pathology is studied, whereas, in the late stage of AD, the pathology becomes complicated with additional contributions of Tau, necroptosis, etc., which are not present in the mouse model. Indeed, the pathology in mouse models is considered to reflect earlier phases of disease (Ashe and Zahs, 2010). Between the appearance of amyloid plaques and neuronal tangles in the human brain to the ultimate dementia in patients, up to 20 years may elapse (Bateman et al., 2012; Villemagne et al., 2013; Jansen et al., 2015). Thus, many additional changes will have occurred since initiation of the amyloid pathology in humans. Nevertheless, many of the genes identified in the PIG and OLIG modules in the mouse display significant changes in late-stage AD.

DISCUSSION

We used two technologies, ST (Stahl et al., 2016) and ISS (Qian et al., 2020), to study the cellular phase of AD (De Strooper and Karran, 2016). We generated a large dataset (<https://www.alzmap.org/>) of transcriptional changes in the mouse and human brain as a function of increasing amyloid pathology. Here we focused on the transcriptomic changes in the immediate neighborhood of amyloid plaques; i.e., in a circle with a 100- μ m diameter. We leave open the discussion of what form of A β might trigger the pathological changes; some groups have suggested that a toxic halo of oligomeric A β surrounding amyloid plaques is the bioactive agent (Koffie et al., 2009; Mucke and Selkoe, 2012).

We show, in a well-studied *App* knockin mouse model (Saito et al., 2014), gradual establishment of a multicellular co-expressed gene response encompassing 57 PIGs in the microenvironments of amyloid plaques (Figure 5). The PIGs represent intercellular crosstalk between astrocytes and microglia and involve other cells. This interplay results in concomitant alterations in the classical complement system and endosomal/lysosomal pathways. The data bring together several pathways that have been implicated separately in AD. We also describe a dynamic OLIG response largely representing myelin-related genes of oligodendrocytes and modulated by gradual amyloid accumulation (Figure 6). In contrast to the rather homogeneous PIGs response (Figure 3B), the OLIG response varies between different brain regions (Figure 6C). ISS of more than 200 human genes, including PIGs and OLIGs in the frontal cortical lobe, partially strengthens our observations (Figure 7).

We refer to the accompanying website (<https://www.alzmap.org/>), where all data and bioinformatics pipelines are provided. There we show all modules defined by WGCNA, including three neuronal modules (magenta, brown, and pink), an astroglial-vascular module (black), and a protein translation module (yellow), which is, interestingly, also modulated along the A β axis (Figure S3B). Further information regarding the dysregulation of lipid metabolism, the mitogen-activated protein kinase (MAPK) cascade, synapses, ion channels, and the mitochondrial respiratory chain supporting the GO category analysis in Figure S3A is also available there.

ST and ISS to Probe the Multicellular Environment of Amyloid Plaques

The main data supporting our conclusions are derived from the ST (Stahl et al., 2016) analysis of 10 control and 10 diseased coronal slices of mice at different ages, encompassing more than 10,000 small brain volumes ($8 \times 10^{-5} \text{ mm}^3$). It is clear that the available ST technology does not reach single-cell level. To increase cellular resolution, we combined this unbiased approach with additional *in situ* hybridization using RNAscope and multi-molecule ISS (Qian et al., 2020). We performed ISS on 4 coronal sections of mice and on 6 sections of the human superior frontal gyrus. These *in situ* experiments confirm, in general, the predictions made from the unbiased ST approach in the mouse (Figures 2D and 4E). Although the technologies used here do not require harsh dissociation procedures like single-cell or single-nucleus approaches and maintain spatial information, the lack of single-cell resolution with ST and the low sensitivity of ISS requires further technological improvements (Eng et al., 2019; Rodrigues et al., 2019; Vickovic et al., 2019; Stickels et al., 2020). Nevertheless, our data show that the combination of ST and ISS is useful in the study of neurological disease. This first study opens a new way of investigating the pathology of AD at a genome-wide scale, complementing the *in situ* hybridization or immunohistochemistry approaches that have directed the field for more than a century.

Complement as an Important Part of the Intercellular Crosstalk in the Amyloid Plaques

Inappropriate control of the classical complement cascade causes unresolvable inflammation and disease (Hong et al., 2016; Hansen et al., 2018; Morgan, 2018). The classical

complement cascade is triggered by C1q-complex, and C1q is strongly expressed by microglia and enriched in the plaque cellular niche, as shown in Figures 4I and S4B (Eikelenboom et al., 1989; McGeer et al., 1989). The release of C1q from microglia is necessary to induce neurotoxic, inflammatory astrocytes (A1) (Liddelow et al., 2017), which also strongly upregulate genes involved in classical complement activation, such as *C4* (Figures 4I and S4B; Zamanian et al., 2012). Interestingly, activation of C1Q can be attenuated by another molecule of the PIG network, APOE (Yin et al., 2019). An exciting finding is illustrated in Figure 5, demonstrating how the overall connectivity between the PIGs is low in WT brains and increases with A β load in *App^{NL-G-F}* brains. The genes with strongest connections between the 3 PIG clusters are *ApoE*, *B2m*, and *Ctsd* from the green cluster; *C1qa*, *C1qb*, *C1qc*, and *Ctss* from the blue cluster; and *Trem2* and *Tyrobp* from the orange cluster. We propose that the network of 57 PIGs constitutes a coordinated cellular response to plaques, especially between astrocytes and microglia, via microglial signaling of secreted proteins like C1Q and APOE and receptors like TREM2 and the associated TYROBP, which overall results in astroglial activation (e.g., *Gfap*, *C4*, *Clu*, *Prdx6*, *Cst3*, and *Serpina3*) in the vicinity of amyloid plaques. This response results, among others, in inappropriate control of the classical complement cascade. We confirm enrichment of several complement components (*C1QA*, *C1QB*, *C1QC*, and *CLU*) and an adaptor of TREM2, *TYROBP*, around amyloid plaques in AD patients (Figure 7D). More investigations of the interplay of APOE-TREM2 (Krasemann et al., 2017; Parhizkar et al., 2019) with the complement pathway (Yin et al., 2019) are required to understand how the inflammation driven by the complement cascade in AD can be exploited therapeutically.

Oligodendrocytes Are Part of the Cellular Phase in Amyloid Plaques

The response of oligodendrocytes to amyloid plaques is of high interest (Braak and Braak, 1996; De Strooper and Karran, 2016). Oligodendrocytes are the largest group of non-neuronal cells in the brain and are vulnerable, decreasing ~25% in the aging brain (Pelvig et al., 2008). Age-associated myelin breakdown is seen in MRI scans of patients from age 50 on, which is accentuated in APOE4 patients (Scheltens et al., 1992; Bartzokis, 2011). However, single-cell transcriptomics experiments have recently shown a positive correlation of AD pathology with increased expression of genes responsible for myelination in oligodendrocytes in AD patients (Grubman et al., 2019; Mathys et al., 2019). APP-overexpressing transgenic mice exhibit increased thickness of myelin (Xu et al., 2014) and contain more oligodendrocytes (Zhou et al., 2020). In our study, the OLIG module, strongly enriched for genes involved in myelin processing, is, in general, initially upregulated in *App^{NL-G-F}* versus WT mice but becomes downregulated in microenvironments with the highest A β accumulation. We speculate that upregulation of OLIG might have a protective role that ultimately fails with increasing amyloid plaque load.

Several studies have recently reported involvement of oligodendrocyte lineages in inflammation of demyelinating diseases, such as multiple sclerosis (Falcão et al., 2018; Kirby et al., 2019) and AD (Zhang et al., 2019; Zhou et al., 2020). Zhang et al. (2019)

suggested that oligodendrocyte precursor cells (OPCs) surrounding amyloid plaques undergo senescence and stop differentiating into myelin-repairing oligodendrocytes. Instead, they release inflammatory molecules into the plaque environment (Zhang et al., 2019). Zhou et al. (2020) reported an oligodendrocyte A β -reactive state that increases expression of *C4*, *Serpina3n*, and *H2-D1*. In our study, those three A β -reactive oligodendroglial markers are part of the PIGs, and the expression of *C4* is increased in oligodendrocytes close to amyloid plaques (Figures 4H and S4B). Together with activated astrocytes and microglia, oligodendrocytes are clearly part of the multicellular inflammatory environment of amyloid plaques. Further work is now needed to explore the potential of therapies targeted at oligodendrocyte lineages for AD.

Reproducibility of PIGs and OLIGs across Mouse Models and Human Diseases

Several transcriptomic studies have suggested diverse gene-regulatory networks related to amyloid or tau pathology (Sierksma et al., 2020), late-onset AD (LOAD) (Zhang et al., 2013), cognitive decline (Mostafavi et al., 2018), amyotrophic lateral sclerosis (ALS) (Maniatis et al., 2019), frontotemporal dementia (FTD) (Swarup et al., 2019), and other brain disorders. We compared our WGCNA-identified networks with previously published transcriptomics studies (Table S7).

Mostafavi et al. (2018) and Zhang et al. (2013) provide bulk sequencing data on large cohorts of human brains. Mostafavi et al. (2018) compared five phenotypes related to AD, including A β burden. The most correlated module with A β burden, m109, is strongly enriched with neuronal genes and strongly associated with cognitive decline. m109 has no significant overlaps with our PIGs and OLIGs, which is not unexpected, being a neuronal network. m109, however, significantly overlaps with our blue module (logged odds ratio [LOR] = 1.11, *padj* = $1.37e^{-15}$). In contrast, the PIG module significantly overlaps with their microglial m116 module (LOR = 3.69, *padj* = $2.61e^{-17}$) and the OLIG module with their oligodendroglial m110 module (LOR = 3.73, *padj* = $1.15e^{-55}$). Although m116 does not show significant correlation with any of the AD phenotypes in Mostafavi et al. (2018), m116 is associated with AD diagnosis in another human cohort (Zhang et al., 2013). Zhang et al. (2013) constructed gene-regulatory networks from 1,647 post-mortem brain tissues from LOAD patients and controls and correlated networks with 26 neuropathological traits, such as Braak stage and brain atrophy. In the top 20 modules ranked for relevance to LOAD pathology, the immune-related “yellow” module has a strong overlap with the PIG module (LOR = 2.59, *padj* = $2.26e^{-11}$) and the myelination-associated light green module with the OLIG module (LOR = 3.82, *padj* = $2.62e^{-58}$). In addition, the PIGs-associated yellow module is identified as the strongest gain-of-connectivity module, whereas the OLIG-associated light green module is identified as one of the loss-of-connectivity modules in the Zhang et al. (2013). This result is in line with our observation of increased network connectivity in the PIGs (Figure 5) and decreased connectivity in the OLIGs (Figure S5B) and further indicates their relevance to LOAD.

We further made a comparison with a study that used two mouse models, one for amyloid and one for tau pathology

(Sierksma et al., 2020). The module most strongly overlapping with our PIGs module is the APPtg blue module (LOR = 3.57, $\text{padj} = 2.07e^{-27}$), which is enriched with AD risk genes and is a microglial response to amyloid rather than tau pathology. Our OLIG module has a strong overlap with the APPtg-greenyellow module (LOR = 4.11, $\text{padj} = 7.63e^{-28}$), which is an oligodendroglial response in the amyloid but not the tau model. This observation is in line with our hypothesis that OLIG is an oligodendroglia-related response to mild A β exposure, whereas PIGs is an A β plaque-induced co-expression network, and further suggests a minimal correlation of amyloid-responsive networks to tau pathology.

We finally compared data from an ALS (Maniatis et al., 2019) and an FTD study (Swarup et al., 2019). Maniatis et al. (2019) provided comprehensive characterization of transcriptional changes in spinal cords of an ALS mouse model and patients. The co-expression networks are cell-type-annotated at the level of submodule levels. The PIG module significantly overlaps with microglial submodule 8.17 (LOR = 4.95, $\text{padj} = 5.93e^{-39}$) in this ALS study, containing *Tyrobp*, *Trem2*, *C1q*, and other reactive microglial genes. One of the submodules in the PIGs, the astroglial green cluster, has a mild overlap with their astroglial submodule 8.9 (LOR = 4.07, $\text{padj} = 0.016$), containing *Gfap*, *ApoE*, and *Prdx6*. The OLIG module overlaps with their mature oligodendrocyte submodule 8.18 (LOR = 3.52, $\text{padj} = 3.84e^{-05}$). The overlap of PIGs and OLIGs with their module 8 glia indicates the overlap in the glial responses between AD and ALS. Interestingly, these authors also showed that the dysregulation of module 8 can be rescued by ablation of autophagy in neurons in *Atg7* cKO mice (Maniatis et al., 2019). The PIGs network also highlights auto-lysosomal pathways in neurons and inflammatory gliosis.

Swarup et al. (2019) identified two major neurodegeneration-associated modules in FTD mouse models. They identified a neurodegeneration-associated inflammatory module (NAI) and a synaptic (NAS) module that are also dysregulated in human FTD, AD, and ALS samples but not in human major depressive disorder, schizophrenia, or bipolar disorder samples. The NAS module significantly overlapped with our neuronal brown (LOR = 1.03, $\text{padj} = 5.68e^{-11}$) and magenta modules (LOR = 1.51, $\text{padj} = 2.80e^{-05}$) (Figure S3). The magenta module is downregulated in response to amyloid plaques, whereas the brown module does not change (Figure S3B). This shows that our data separate the co-expression network in response to amyloid plaques from the more general neurodegeneration effect captured in the NAS module. The glia-enriched NAI module shows a significant overlap with our PIG module (LOR = 2.41, $\text{padj} = 1.21e^{-15}$) and OLIG module (LOR = 2.61, $\text{padj} = 1.07e^{-54}$). This conclusion nicely aligns with the observations described by Maniatis et al. (2019), which also point out the overlap in glial responses between neurodegenerative diseases. In addition, the NAI module also shows a significant enrichment with our blue module (LOR = 0.74, $\text{padj} = 1.14e^{-46}$). There are, in total, 31 genes overlapping between our blue module, the m109 module, and the NAI module, including genes encoding for regulators of ubiquitin-mediated proteolysis (*Ubr5*), the nuclear factor κ B (NF- β B) signaling pathway (*Ikbkb*) and the Wnt signaling pathway (*Dvl2*). We suggest that the blue module indi-

cates a more generic response in neurodegeneration that operates in addition to plaque-reactive networks, such as the PIGs.

Conclusions

Here we demonstrate a brain disease-oriented application of the recently developed ST (Ståhl et al., 2016) and ISS (Qian et al., 2020) technologies. The data demonstrate that amyloid plaques are not innocent bystanders of the disease, as sometimes suggested (Robakis, 2010; Kametani and Hasegawa, 2018), but, in fact, induce a strong and coordinated response of all cell types in the amyloid plaque cellular niche (De Strooper and Karran, 2016). Further work is needed to understand whether and when removal of amyloid plaques (for instance, by immunization; Gallardo and Holtzman, 2017) is sufficient to reverse these ongoing cellular processes. It is tempting to speculate that antibody binding to amyloid plaques would modulate these glial responses, which would complicate interpretation of outcomes of clinical trials because these cellular effects might be different with different antibodies (Gallardo and Holtzman, 2017; Schneider, 2020).

STAR★METHODS

Detailed methods are provided in the online version of this paper and include the following:

- KEY RESOURCES TABLE
- RESOURCE AVAILABILITY
 - Lead Contact
 - Materials Availability
 - Data and Code Availability
- EXPERIMENTAL MODEL AND SUBJECT DETAILS
 - Mice
 - Human
- METHOD DETAILS
 - Tissue collection for Spatial Transcriptomics
 - *In situ* 2D-RNaseq via Spatial Transcriptomics
 - Immunohistochemistry of Spatial Transcriptomics
 - *In situ* sequencing and immunostaining of mouse samples
 - *In situ* sequencing and immunostaining of human samples
 - Multiplexing RNAscope and immunohistochemistry
- QUANTIFICATION AND STATISTICAL ANALYSIS
 - Image analysis
 - Sequencing Data Analysis
- ADDITIONAL RESOURCES

SUPPLEMENTAL INFORMATION

Supplemental Information can be found online at <https://doi.org/10.1016/j.cell.2020.06.038>.

ACKNOWLEDGMENTS

This work was supported by INSTALZ (EU), the EU Joint Program (JPND), Fonds voor Wetenschappelijk Onderzoek (FWO, Belgium), "Methusalem" and "Opening the Future" grants from KU Leuven (Belgium), Stichting Alzheimer Onderzoek (Belgium), the Alzheimer Association (USA), the MRC

(UK), the Alzheimer Society (UK), Alzheimer Research UK, VIB Tech Watch (Belgium), the Knut and Alice Wallenberg Foundation (Sweden), and the Thon Foundation (Sweden). W.-T.C. is supported by the Taiwan Ministry of Science and Technology (MOST-105-2917-I-564-081) and Marie Skłodowska-Curie agreement no. 665501. S.M. and imaging is supported by FWO and KUL. B.D.S. is supported by the European Research Council ERC-CELL-PHASE_AD834682 (EU), Geneeskundige Stichting Koningin Elisabeth (Belgium), and Bax-Vanluffelen (Belgium).

AUTHOR CONTRIBUTIONS

W.-T.C., A.L., M.F., and B.D.S. conceptualized and designed the study. K.C., A.S., C.S.F., and W.-T.C. optimized and performed ST together with inventors A.J., J.F.N., and J. Lundberg. X.Q., J. Laláková, M.K., and W.-T.C. optimized and performed ISS. W.-T.C. performed and analyzed *in situ* hybridization (RNAscope) with I.V., L.W., and N.C. W.-T.C. and B.P. optimized image analysis of ST with J.F.N. and image analysis of ISS with X.Q. along with data analysis input from M.F. B.P. developed programs for image analysis of ST and ISS. N.C. developed GA3 protocols for RNAscope quantification. S.M. and N.C. set up slide scanner image acquisition. R.M., E.S., and S.B. assisted with the experiments. A.L. and M.F. conceptualized and executed all bioinformatics analysis with biological input from W.-T.C. and B.D.S. M.F. and A.L. developed <https://www.alzmap.org/>. T.C.S. contributed animals. I.H. contributed human materials. B.D.S. was responsible for funding. The first draft of the manuscript was written by W.-T.C., A.L., M.F., and B.D.S. with input from all co-authors. All co-authors read and approved the final version of the manuscript.

DECLARATION OF INTERESTS

X.Q., J.L., and M.K. are employees of CARTANA AB. A.J. is an employee of, J.L. is a scientific advisor for, and J.F.N. has an IP agreement with 10X Genomics. B.D.S. is consultant for several companies but has no COI with the current manuscript. All other authors declare no competing interests.

Received: August 1, 2019

Revised: April 17, 2020

Accepted: June 25, 2020

Published: July 22, 2020

SUPPORTING CITATIONS

The following references appear in the Supplemental Information: Artegiani et al. (2017); Batiuk et al. (2020); Bennett et al. (2016); Doorn et al. (2015); Färber et al. (2009); Habib et al. (2017); Hackett (2018); Hodge et al. (2019); Horti et al. (2019); Li et al. (2019a); McKenzie et al. (2018); Pittman Elmore et al. (2015); Rusnakova et al. (2013); Schäfer et al. (2000); Sun et al. (2017); Tasic et al. (2018); Usoskin et al. (2015); Zhang et al. (2014); Zhang et al. (2016).

REFERENCES

Artegiani, B., Lyubimova, A., Muraro, M., van Es, J.H., van Oudenaarden, A., and Clevers, H. (2017). A Single-Cell RNA Sequencing Study Reveals Cellular and Molecular Dynamics of the Hippocampal Neurogenic Niche. *Cell Rep.* *21*, 3271–3284.

Ashe, K.H., and Zahs, K.R. (2010). Probing the biology of Alzheimer's disease in mice. *Neuron* *66*, 631–645.

Bankhead, P., Loughrey, M.B., Fernández, J.A., Dombrowski, Y., McArt, D.G., Dunne, P.D., McQuaid, S., Gray, R.T., Murray, L.J., Coleman, H.G., et al. (2017). QuPath: Open source software for digital pathology image analysis. *Sci. Rep.* *7*, 16878.

Bartzokis, G. (2011). Alzheimer's disease as homeostatic responses to age-related myelin breakdown. *Neurobiol. Aging* *32*, 1341–1371.

Bateman, R.J., Xiong, C., Benzinger, T.L., Fagan, A.M., Goate, A., Fox, N.C., Marcus, D.S., Cairns, N.J., Xie, X., Blazey, T.M., et al.; Dominantly Inherited

Alzheimer Network (2012). Clinical and biomarker changes in dominantly inherited Alzheimer's disease. *N. Engl. J. Med.* *367*, 795–804.

Batiuk, M.Y., Martirosyan, A., Wahis, J., de Vin, F., Marneffe, C., Kusserow, C., Koeppen, J., Viana, J.F., Oliveira, J.F., Voet, T., et al. (2020). Identification of region-specific astrocyte subtypes at single cell resolution. *Nat. Commun.* *11*, 1220.

Bennett, M.L., Bennett, F.C., Liddel, S.A., Ajami, B., Zamanian, J.L., Fernhoff, N.B., Mulinylaw, S.B., Bohlen, C.J., Adil, A., Tucker, A., et al. (2016). New tools for studying microglia in the mouse and human CNS. *Proc. Natl. Acad. Sci. USA* *113*, E1738–E1746.

Bhatia, S., Kim, W.S., Shepherd, C.E., and Halliday, G.M. (2019). Apolipoprotein D Upregulation in Alzheimer's Disease but Not Frontotemporal Dementia. *J. Mol. Neurosci.* *67*, 125–132.

Borowsky, I.W., and Collins, R.C. (1989). Histochemical changes in enzymes of energy metabolism in the dentate gyrus accompany deafferentation and synaptic reorganization. *Neuroscience* *33*, 253–262.

Braak, H., and Braak, E. (1991). Neuropathological staging of Alzheimer-related changes. *Acta Neuropathol.* *82*, 239–259.

Braak, H., and Braak, E. (1996). Development of Alzheimer-related neurofibrillary changes in the neocortex inversely recapitulates cortical myelogenesis. *Acta Neuropathol.* *92*, 197–201.

De Strooper, B., and Karran, E. (2016). The Cellular Phase of Alzheimer's Disease. *Cell* *164*, 603–615.

Del-Aguila, J.L., Li, Z., Dube, U., Mihindukulasuriya, K.A., Budde, J.P., Fernandez, M.V., Ibanez, L., Bradley, J., Wang, F., Bergmann, K., et al. (2019). A single-nuclei RNA sequencing study of Mendelian and sporadic AD in the human brain. *Alzheimers Res. Ther.* *11*, 71.

Doorn, K.J., Brevé, J.J., Drukarch, B., Boddeke, H.W., Huitinga, I., Lucassen, P.J., and van Dam, A.M. (2015). Brain region-specific gene expression profiles in freshly isolated rat microglia. *Front. Cell. Neurosci.* *9*, 84.

Eden, E., Navon, R., Steinfeld, I., Lipson, D., and Yakhini, Z. (2009). GOrilla: a tool for discovery and visualization of enriched GO terms in ranked gene lists. *BMC Bioinformatics* *10*, 48.

Eikelenboom, P., Hack, C.E., Rozemuller, J.M., and Stam, F.C. (1989). Complement activation in amyloid plaques in Alzheimer's dementia. *Virchows Arch. B Cell Pathol. Incl. Mol. Pathol.* *56*, 259–262.

Eng, C.L., Lawson, M., Zhu, Q., Dries, R., Koulana, N., Takei, Y., Yun, J., Cronin, C., Karp, C., Yuan, G.C., and Cai, L. (2019). Transcriptome-scale super-resolved imaging in tissues by RNA seqFISH. *Nature* *568*, 235–239.

Falcão, A.M., van Bruggen, D., Marques, S., Meijer, M., Jäkel, S., Agirre, E., Samudiyata, Floriddia, E.M., Vanichkina, D.P., Ffrench-Constant, C., et al. (2018). Disease-specific oligodendrocyte lineage cells arise in multiple sclerosis. *Nat. Med.* *24*, 1837–1844.

Färber, K., Cheung, G., Mitchell, D., Wallis, R., Weihe, E., Schwaebler, W., and Kettenmann, H. (2009). C1q, the recognition subcomponent of the classical pathway of complement, drives microglial activation. *J. Neurosci. Res.* *87*, 644–652.

Gallardo, G., and Holtzman, D.M. (2017). Antibody therapeutics targeting A β and tau. *Cold Spring Harb. Perspect. Med.* *7*, a024331.

Grubman, A., Chew, G., Ouyang, J.F., Sun, G., Choo, X.Y., McLean, C., Simmons, R.K., Buckberry, S., Vargas-Landin, D.B., Poppe, D., et al. (2019). A single-cell atlas of entorhinal cortex from individuals with Alzheimer's disease reveals cell-type-specific gene expression regulation. *Nat. Neurosci.* *22*, 2087–2097.

Habib, N., Avraham-Davidi, I., Basu, A., Burks, T., Shekhar, K., Hofree, M., Choudhury, S.R., Aguet, F., Gelfand, E., Ardlie, K., et al. (2017). Massively parallel single-nucleus RNA-seq with DroNc-seq. *Nat. Methods* *14*, 955–958.

Hackett, T.A. (2018). Adenosine A₁ Receptor mRNA Expression by Neurons and Glia in the Auditory Forebrain. *Anat. Rec. (Hoboken)* *301*, 1882–1905.

Hansen, D.V., Hanson, J.E., and Sheng, M. (2018). Microglia in Alzheimer's disease. *J. Cell Biol.* *217*, 459–472.

- Hodge, R.D., Bakken, T.E., Miller, J.A., Smith, K.A., Barkan, E.R., Graybiuck, L.T., Close, J.L., Long, B., Johansen, N., Penn, O., et al. (2019). Conserved cell types with divergent features in human versus mouse cortex. *Nature* 573, 61–68.
- Hong, S., Beja-Glasser, V.F., Nfonoyim, B.M., Frouin, A., Li, S., Ramakrishnan, S., Merry, K.M., Shi, Q., Rosenthal, A., Barres, B.A., et al. (2016). Complement and microglia mediate early synapse loss in Alzheimer mouse models. *Science* 352, 712–716.
- Horti, A.G., Naik, R., Foss, C.A., Minn, I., Misheneva, V., Du, Y., Wang, Y., Mathews, W.B., Wu, Y., Hall, A., et al. (2019). PET imaging of microglia by targeting macrophage colony-stimulating factor 1 receptor (CSF1R). *Proc. Natl. Acad. Sci. USA* 116, 1686–1691.
- Huber, W., Carey, V.J., Gentleman, R., Anders, S., Carlson, M., Carvalho, B.S., Bravo, H.C., Davis, S., Gatto, L., Girke, T., et al. (2015). Orchestrating high-throughput genomic analysis with Bioconductor. *Nat. Methods* 12, 115–121.
- Jansen, I.E., Savage, J.E., Watanabe, K., Bryois, J., Williams, D.M., Steinberg, S., Sealock, J., Karlsson, I.K., Hägg, S., Athanasiu, L., et al. (2019). Genome-wide meta-analysis identifies new loci and functional pathways influencing Alzheimer's disease risk. *Nat. Genet.* 51, 404–413.
- Jansen, W.J., Ossenkuppe, R., Knol, D.L., Tijms, B.M., Scheltens, P., Verhey, F.R., Visser, P.J., Aalten, P., Aarsland, D., Alcolea, D., et al.; Amyloid Biomarker Study Group (2015). Prevalence of cerebral amyloid pathology in persons without dementia: a meta-analysis. *JAMA* 313, 1924–1938.
- Kametani, F., and Hasegawa, M. (2018). Reconsideration of amyloid hypothesis and tau hypothesis in Alzheimer's disease. *Front. Neurosci.* 12, 25.
- Karran, E., Mercken, M., and De Strooper, B. (2011). The amyloid cascade hypothesis for Alzheimer's disease: an appraisal for the development of therapeutics. *Nat. Rev. Drug Discov.* 10, 698–712.
- Ke, R., Mignardi, M., Pacureanu, A., Svedlund, J., Botling, J., Wählby, C., and Nilsson, M. (2013). In situ sequencing for RNA analysis in preserved tissue and cells. *Nat. Methods* 10, 857–860.
- Keren-Shaul, H., Spinrad, A., Weiner, A., Matcovitch-Natan, O., Dvir-Szternfeld, R., Ulland, T.K., David, E., Baruch, K., Lara-Astaiso, D., Toth, B., et al. (2017). A Unique Microglia Type Associated with Restricting Development of Alzheimer's Disease. *Cell* 169, 1276–1290.e17.
- Kirby, L., Jin, J., Cardona, J.G., Smith, M.D., Martin, K.A., Wang, J., Strasburger, H., Herbst, L., Alexis, M., Karnell, J., et al. (2019). Oligodendrocyte precursor cells present antigen and are cytotoxic targets in inflammatory demyelination. *Nat. Commun.* 10, 3887.
- Koffie, R.M., Meyer-Luehmann, M., Hashimoto, T., Adams, K.W., Mielke, M.L., Garcia-Alloza, M., Mischeva, K.D., Smith, S.J., Kim, M.L., Lee, V.M., et al. (2009). Oligomeric amyloid β associates with postsynaptic densities and correlates with excitatory synapse loss near senile plaques. *Proc. Natl. Acad. Sci. USA* 106, 4012–4017.
- Krasemann, S., Madore, C., Cialic, R., Baufeld, C., Calcagno, N., El Fatimy, R., Beckers, L., O'Loughlin, E., Xu, Y., Fanek, Z., et al. (2017). The TREM2-APOE Pathway Drives the Transcriptional Phenotype of Dysfunctional Microglia in Neurodegenerative Diseases. *Immunity* 47, 566–581.e9.
- Lake, B.B., Codeluppi, S., Yung, Y.C., Gao, D., Chun, J., Kharchenko, P.V., Linnarsson, S., and Zhang, K. (2017). A comparative strategy for single-nucleus and single-cell transcriptomes confirms accuracy in predicted cell-type expression from nuclear RNA. *Sci. Rep.* 7, 6031.
- Legland, D., Arganda-Carreras, I., and Andrey, P. (2016). MorphoLibJ: integrated library and plugins for mathematical morphology with ImageJ. *Bioinformatics* 32, 3532–3534.
- Lein, E.S., Hawrylycz, M.J., Ao, N., Ayres, M., Bensinger, A., Bernard, A., Boe, A.F., Boguski, M.S., Brockway, K.S., Byrnes, E.J., et al. (2006). Genome-wide atlas of gene expression in the adult mouse brain. *Nature* 445, 168–176.
- Li, Q., Cheng, Z., Zhou, L., Darmanis, S., Neff, N.F., Okamoto, J., Gulati, G., Bennett, M.L., Sun, L.O., Clarke, L.E., et al. (2019a). Developmental Heterogeneity of Microglia and Brain Myeloid Cells Revealed by Deep Single-Cell RNA Sequencing. *Neuron* 101, 207–223.e10.
- Liddel, S.A., Guttenplan, K.A., Clarke, L.E., Bennett, F.C., Bohlen, C.J., Schirmer, L., Bennett, M.L., Münch, A.E., Chung, W.S., Peterson, T.C., et al. (2017). Neurotoxic reactive astrocytes are induced by activated microglia. *Nature* 541, 481–487.
- Long, J.M., and Holtzman, D.M. (2019). Alzheimer Disease: An Update on Pathobiology and Treatment Strategies. *Cell* 179, 312–339.
- Maniatis, S., Äijö, T., Vickovic, S., Braine, C., Kang, K., Mollbrink, A., Fagegaltier, D., Andrusivová, Ž., Saarenpää, S., Saiz-Castro, G., et al. (2019). Spatio-temporal dynamics of molecular pathology in amyotrophic lateral sclerosis. *Science* 364, 89–93.
- Matarin, M., Salih, D.A., Yasvoina, M., Cummings, D.M., Guelfi, S., Liu, W., Nahaboo Solim, M.A., Moens, T.G., Paublete, R.M., Ali, S.S., et al. (2015). A genome-wide gene-expression analysis and database in transgenic mice during development of amyloid or tau pathology. *Cell Rep.* 10, 633–644.
- Mathys, H., Davila-Velderrain, J., Peng, Z., Gao, F., Mohammadi, S., Young, J.Z., Menon, M., He, L., Abdurrob, F., Jiang, X., et al. (2019). Single-cell transcriptomic analysis of Alzheimer's disease. *Nature* 570, 332–337.
- McGeer, P.L., Akiyama, H., Itagaki, S., and McGeer, E.G. (1989). Activation of the classical complement pathway in brain tissue of Alzheimer patients. *Neurosci. Lett.* 107, 341–346.
- McKenzie, A.T., Wang, M., Hauberg, M.E., Fullard, J.F., Kozlenkov, A., Keenan, A., Hurd, Y.L., Dracheva, S., Casaccia, P., Roussos, P., and Zhang, B. (2018). Brain Cell Type Specific Gene Expression and Co-expression Network Architectures. *Sci. Rep.* 8, 8868.
- Morgan, B.P. (2018). Complement in the pathogenesis of Alzheimer's disease. *Semin. Immunopathol.* 40, 113–124.
- Mostafavi, S., Gaiteri, C., Sullivan, S.E., White, C.C., Tasaki, S., Xu, J., Taga, M., Klein, H.U., Patrick, E., Komashko, V., et al. (2018). A molecular network of the aging human brain provides insights into the pathology and cognitive decline of Alzheimer's disease. *Nat. Neurosci.* 21, 811–819.
- Mucke, L., and Selkoe, D.J. (2012). Neurotoxicity of amyloid β -protein: synaptic and network dysfunction. *Cold Spring Harb. Perspect. Med.* 2, a006338.
- Navarro, J.F., Sjöstrand, J., Salmén, F., Lundberg, J., and Ståhl, P.L. (2017). ST Pipeline: an automated pipeline for spatial mapping of unique transcripts. *Bioinformatics* 33, 2591–2593.
- Parhizkar, S., Arzberger, T., Brendel, M., Kleinberger, G., Deussing, M., Focke, C., Nuscher, B., Xiong, M., Ghasemigharagou, A., Katzmarzki, N., et al. (2019). Loss of TREM2 function increases amyloid seeding but reduces plaque-associated ApoE. *Nat. Neurosci.* 22, 191–204.
- Pelvig, D.P., Pakkenberg, H., Stark, A.K., and Pakkenberg, B. (2008). Neocortical glial cell numbers in human brains. *Neurobiol. Aging* 29, 1754–1762.
- Pittman Elmore, M.R., Najafi, A.R., Koike, M.A., Dagher, N.N., Spangenberg, E.E., Rice, A.R., Kitazawa, M., Matusow, B., Nguyen, H., West, B.L., and Green, K.N. (2015). CSF1 receptor signaling is necessary for microglia viability, which unmasks a cell that rapidly repopulates the microglia-depleted adult brain. *Neuron* 82, 380–397.
- Qian, X., Harris, K.D., Hauling, T., Nicoloutsopoulos, D., Muñoz-Manchado, A.B., Skene, N., Hjerling-Leffler, J., and Nilsson, M. (2020). Probabilistic cell typing enables fine mapping of closely related cell types in situ. *Nat. Methods* 17, 101–106.
- Robakis, N.K. (2010). Are Abeta and its derivatives causative agents or innocent bystanders in AD? *Neurodegener. Dis.* 7, 32–37.
- Robinson, M.D., McCarthy, D.J., and Smyth, G.K. (2010). edgeR: a Bioconductor package for differential expression analysis of digital gene expression data. *Bioinformatics* 26, 139–140.
- Rodrigues, S.G., Stickels, R.R., Goeva, A., Martin, C.A., Murray, E., Vanderburg, C.R., Welch, J., Chen, L.M., Chen, F., and Macosko, E.Z. (2019). Slide-seq: A scalable technology for measuring genome-wide expression at high spatial resolution. *Science* 363, 1463–1467.
- Rusnakova, V., Honsa, P., Dzamba, D., Ståhlberg, A., Kubista, M., and Anderova, M. (2013). Heterogeneity of astrocytes: from development to injury - single cell gene expression. *PLoS ONE* 8, e69734.

- Saito, T., Matsuba, Y., Mihira, N., Takano, J., Nilsson, P., Itoharu, S., Iwata, N., and Saido, T.C. (2014). Single App knock-in mouse models of Alzheimer's disease. *Nat. Neurosci.* *17*, 661–663.
- Sala Frigerio, C., Wolfs, L., Fattorelli, N., Thrupp, N., Voytyuk, I., Schmidt, I., Mancuso, R., Chen, W.T., Woodbury, M.E., Srivastava, G., et al. (2019). The Major Risk Factors for Alzheimer's Disease: Age, Sex, and Genes Modulate the Microglia Response to A β Plaques. *Cell Rep.* *27*, 1293–1306.e6.
- Salih, D.A., Bayram, S., Guelfi, M.S., Reynolds, R., Shoai, M., Rytén, M., Brenton, J., Zhang, D., Matarin, M., Botia, J., et al. (2018). Genetic variability in response to A β deposition influences Alzheimer's risk. *bioRxiv*. <https://doi.org/10.1101/437657>.
- Schäfer, M.K.-H., Schwaible, W.J., Post, C., Salvati, P., Calabresi, M., Sim, R.B., Petry, F., Loos, M., and Weihe, E. (2000). Complement C1q is dramatically up-regulated in brain microglia in response to transient global cerebral ischemia. *J. Immunol.* *164*, 5446–5452.
- Scheltens, P., Barkhof, F., Valk, J., Algra, P.R., van der Hoop, R.G., Nauta, J., and Wolters, E.C. (1992). White matter lesions on magnetic resonance imaging in clinically diagnosed Alzheimer's disease. Evidence for heterogeneity. *Brain* *115*, 735–748.
- Schindelin, J., Arganda-Carreras, I., Frise, E., Kaynig, V., Longair, M., Pietzsch, T., Preibisch, S., Rueden, C., Saalfeld, S., Schmid, B., et al. (2012). Fiji: an open-source platform for biological-image analysis. *Nat. Methods* *9*, 676–682.
- Schmidt, R.E., and Gessner, J.E. (2005). Fc receptors and their interaction with complement in autoimmunity. *Immunol. Lett.* *100*, 56–67.
- Schneider, L. (2020). A resurrection of aducanumab for Alzheimer's disease. *Lancet Neurol.* *19*, 111–112.
- Sevigny, J., Chiao, P., Bussière, T., Weinreb, P.H., Williams, L., Maier, M., Dunstan, R., Salloway, S., Chen, T., Ling, Y., et al. (2016). The antibody aducanumab reduces A β plaques in Alzheimer's disease. *Nature* *537*, 50–56.
- Sierksma, A., Lu, A., Mancuso, R., Fattorelli, N., Thrupp, N., Salta, E., Zoco, J., Blum, D., Buée, L., De Strooper, B., and Fiers, M. (2020). Novel Alzheimer risk genes determine the microglia response to amyloid- β but not to TAU pathology. *EMBO Mol. Med.* *12*, e10606.
- Stähl, P.L., Salmén, F., Vickovic, S., Lundmark, A., Navarro, J.F., Magnusson, J., Giacomello, S., Asp, M., Westholm, J.O., Huss, M., et al. (2016). Visualization and analysis of gene expression in tissue sections by spatial transcriptomics. *Science* *353*, 78–82.
- Stickels, R.R., Murray, E., Kumar, P., Li, J., Marshall, J.L., Di Bella, D., Arlotta, P., Macosko, E.Z., and Chen, F. (2020). Sensitive spatial genome wide expression profiling at cellular resolution. *bioRxiv*. <https://doi.org/10.1101/2020.03.12.989806>.
- Sun, W., Cornwell, A., Li, J., Peng, S., Osorio, M.J., Aalling, N., Wang, S., Benraiss, A., Lou, N., Goldman, S.A., and Nedergaard, M. (2017). SOX9 is an astrocyte-specific nuclear marker in the adult brain outside the neurogenic regions. *J. Neurosci.* *37*, 4493–4507.
- Swarup, V., Hinz, F.I., Rexach, J.E., Noguchi, K.I., Toyoshiba, H., Oda, A., Hirai, K., Sarkar, A., Seyfried, N.T., Cheng, C., et al.; International Frontotemporal Dementia Genomics Consortium (2019). Identification of evolutionarily conserved gene networks mediating neurodegenerative dementia. *Nat. Med.* *25*, 152–164.
- Tasic, B., Yao, Z., Graybiel, L.T., Smith, K.A., Nguyen, T.N., Bertagnolli, D., Goldy, J., Garen, E., Economo, M.N., Viswanathan, S., et al. (2018). Shared and distinct transcriptomic cell types across neocortical areas. *Nature* *563*, 72–78.
- Thal, D.R., Rüb, U., Orantes, M., and Braak, H. (2002). Phases of A β deposition in the human brain and its relevance for the development of AD. *Neurology* *58*, 1791–1800.
- Thielens, N.M., Tedesco, F., Bohlson, S.S., Gaboriaud, C., and Tenner, A.J. (2017). C1q: A fresh look upon an old molecule. *Mol. Immunol.* *89*, 73–83.
- Thrupp, N., Sala Frigerio, C., Wolfs, L., Skene, N.G., Poovathingal, S., Fournier, Y., Matthews, P.M., Theys, T., Mancuso, R., de Strooper, R., and Fiers, M. (2020). Single nucleus sequencing fails to detect microglial activation. *bioRxiv*. <https://doi.org/10.1101/2020.04.13.035386>.
- Usoskin, D., Furlan, A., Islam, S., Abdo, H., Lönnberg, P., Lou, D., Hjerling-Leffler, J., Haeggström, J., Kharchenko, O., Kharchenko, P.V., et al. (2015). Unbiased classification of sensory neuron types by large-scale single-cell RNA sequencing. *Nat. Neurosci.* *18*, 145–153.
- Valdés Hernández, M.D.C., Reid, S., Mikhael, S., and Pernet, C.; Alzheimer's Disease Neuroimaging Initiative (2018). Do 2-year changes in superior frontal gyrus and global brain atrophy affect cognition? *Alzheimers Dement. (Amst.)* *10*, 706–716.
- van den Brink, S.C., Sage, F., Vértesy, Á., Spanjaard, B., Peterson-Maduro, J., Baron, C.S., Robin, C., and van Oudenaarden, A. (2017). Single-cell sequencing reveals dissociation-induced gene expression in tissue subpopulations. *Nat. Methods* *14*, 935–936.
- Vickovic, S., Eraslan, G., Salmén, F., Klughammer, J., Stenbeck, L., Schapiro, D., Åijö, T., Bonneau, R., Bergensträhle, L., Navarro, J.F., et al. (2019). High-definition spatial transcriptomics for in situ tissue profiling. *Nat. Methods* *16*, 987–990.
- Villemagne, V.L., Burnham, S., Bourgeat, P., Brown, B., Ellis, K.A., Salvado, O., Szoek, C., Macaulay, S.L., Martins, R., Maruff, P., et al.; Australian Imaging Biomarkers and Lifestyle (AIBL) Research Group (2013). Amyloid β deposition, neurodegeneration, and cognitive decline in sporadic Alzheimer's disease: a prospective cohort study. *Lancet Neurol.* *12*, 357–367.
- Xu, D.E., Zhang, W.M., Yang, Z.Z., Zhu, H.M., Yan, K., Li, S., Bagnard, D., Dawe, G.S., Ma, Q.H., and Xiao, Z.C. (2014). Amyloid precursor protein at node of Ranvier modulates nodal formation. *Cell Adhes. Migr.* *8*, 396–403.
- Yin, C., Ackermann, S., Ma, Z., Mohanta, S.K., Zhang, C., Li, Y., Nietzsche, S., Westermann, M., Peng, L., Hu, D., et al. (2019). ApoE attenuates unresolvable inflammation by complex formation with activated C1q. *Nat. Med.* *25*, 496–506.
- Zamanian, J.L., Xu, L., Foo, L.C., Nouri, N., Zhou, L., Giffard, R.G., and Barres, B.A. (2012). Genomic analysis of reactive astrogliosis. *J. Neurosci.* *32*, 6391–6410.
- Zeisel, A., Muñoz-Manchado, A.B., Codeluppi, S., Lönnberg, P., La Manno, G., Juréus, A., Marques, S., Munguba, H., He, L., Betsholtz, C., et al. (2015). Brain structure. Cell types in the mouse cortex and hippocampus revealed by single-cell RNA-seq. *Science* *347*, 1138–1142.
- Zhang, B., and Horvath, S. (2005). A general framework for weighted gene co-expression network analysis. *Stat. Appl. Genet. Mol. Biol.* *4*, 17.
- Zhang, B., Gaiteri, C., Bodea, L.G., Wang, Z., McElwee, J., Podtelezniuk, A.A., Zhang, C., Xie, T., Tran, L., Dobrin, R., et al. (2013). Integrated systems approach identifies genetic nodes and networks in late-onset Alzheimer's disease. *Cell* *153*, 707–720.
- Zhang, Y., Chen, K., Sloan, S.A., Bennett, M.L., Scholze, A.R., O'Keefe, S., Phatnani, H.P., Guarnieri, P., Caneda, C., Ruderisch, N., et al. (2014). An RNA-sequencing transcriptome and splicing database of glia, neurons, and vascular cells of the cerebral cortex. *J. Neurosci.* *34*, 11929–11947.
- Zhang, Y., Sloan, S.A., Clarke, L.E., Caneda, C., Plaza, C.A., Blumenthal, P.D., Vogel, H., Steinberg, G.K., Edwards, M.S., Li, G., et al. (2016). Purification and Characterization of Progenitor and Mature Human Astrocytes Reveals Transcriptional and Functional Differences with Mouse. *Neuron* *89*, 37–53.
- Zhang, P., Kishimoto, Y., Grammatikakis, I., Gottimukkala, K., Cutler, R.G., Zhang, S., Abdelmohsen, K., Bohr, V.A., Misra Sen, J., Gorospe, M., and Mattson, M.P. (2019). Senolytic therapy alleviates A β -associated oligodendrocyte progenitor cell senescence and cognitive deficits in an Alzheimer's disease model. *Nat. Neurosci.* *22*, 719–728.
- Zhou, Y., Song, W.M., Andhey, P.S., Swain, A., Levy, T., Miller, K.R., Poliani, P.L., Cominelli, M., Grover, S., Gilfillan, S., et al. (2020). Human and mouse single-nucleus transcriptomics reveal TREM2-dependent and TREM2-independent cellular responses in Alzheimer's disease. *Nat. Med.* *26*, 131–142.

STAR★METHODS

KEY RESOURCES TABLE

REAGENT or RESOURCE	SOURCE	IDENTIFIER
Antibodies		
Alexa Fluor 488 anti- β -amyloid 1-16 6E10, mouse	BioLegend	Cat# 803013; RRID: AB_2564765
anti- β -amyloid 1-16 6E10, mouse	BioLegend	Cat# 803003; RRID: AB_2564652
anti-NeuN, polyclonal guinea pig	Synaptic Systems	Cat# 266004; RRID: AB_2619988
anti-GFAP, rabbit	Dako	Cat# Z0334; RRID: AB_10013382
Alexa-568-conjugated goat anti quinea pig IgG (H+L)	Invitrogen	Cat# A-11075; RRID: AB_2534119
Dylight-647-conjugated goat anti rabbit IgG (H+L)	Invitrogen	Cat# A-21245; RRID: AB_2535813
Atto-488-conjugated goat anti-mouse	Sigma-Aldrich	Cat# 62197; RRID: AB_1137649
Chemicals, Peptides, and Recombinant Proteins		
PFA for RNAscope	affymetrix	19943
ethanol	Fisher Scientific	10428671
D-PBS	Life Technologies	14287072
TrueBlack	Biotium	23007
Formaldehyde 37% for ST	Sigma Aldrich	F8775-25ml
Eosin Y (Aqueous)	Sigma Aldrich	HT110232
SSC (20x)	Sigma Aldrich	S6639
SDS (10x)	Sigma Aldrich	71736
Pepsin, Article	Sigma Aldrich	P7000-25G
Actinomycin D	Sigma Aldrich	A1410-2MG
USERTM Enzyme	Bioké	M5505L
BSA	Bioké	B9000S
M-MuLV Reverse Transcriptase Article	Bioké	M0253L
Cyanine 3-dCTP	PerkinElmer	NEL576001EA
dNTP (10 mM each) Article	Life Technologies	R0191
SuperScript® III Reverse Transcriptase	Life Technologies	18080085
RNaseOUT™ Recombinant Ribonuclease Inhibitor	Life Technologies	10777019
Collagenase (50 U/ μ l)	Life Technologies	17018029
HBSS buffer	Life Technologies	14025050
dATP (100 mM)	Life Technologies	R0141
dGTP (100 mM)	Life Technologies	R0161
dTTP (100 mM)	Life Technologies	R0171
dCTP (100 mM)	Life Technologies	R0151
Second Strand Buffer (5X)	Life Technologies	10812014
PBS - Phosphate-Buffered Saline (10X) pH 7.4	Life Technologies	AM9624
protease K	QIAGEN	19131
bluing buffer	Dako	CS702
hematoxylin	Dako	S3309
Buffer PDK	QIAGEN	1034963
Critical Commercial Assays		
RNA Scope Fluorescent Multiplex Reagents kit v1 including AMP1-4, DAPI	ACDBio	320850
Mm-Cst7 RNAscope probe	ACDBio	498711
Mm-Cd68-C3 RNAscope probe	ACDBio	316611-C3
Mm-C4b RNAscope probe	ACDBio	445161

(Continued on next page)

Continued		
REAGENT or RESOURCE	SOURCE	IDENTIFIER
Mm-C1qa RNAscope probe	ACDBio	441221
Mm-Clu RNAscope probe	ACDBio	427891
Mm-Syp-C3 RNAscope probe	ACDBio	426521-C3
Mm-Mbp-C3 RNAscope probe	ACDBio	451491-C3
Mm-Slc1a3-C3 RNAscope probe	ACDBio	430781-C3
Mm-Itgam-C2 RNAscope probe	ACDBio	311491-C2
Negative Control Probe	ACDBio	320871
RNeasy Micro kit	QIAGEN	74004
ST Library preparation slides	Spatial Transcriptomics	Lot#10001
Deposited Data		
Raw and normalized count matrix of the Spatial Transcriptomics	This paper	GEO: GSE152506
Data and images of <i>in situ</i> sequencing	This paper	https://repo-prod.prod.sagebase.org/repo/v1/doi/locate?id=syn22153884&type=ENTITY
Resource website including sequence data, images, analyses, and resources related to the Spatial Transcriptomics and <i>in situ</i> sequencing of mouse and human samples.	This paper	https://www.alzmap.org/
Experimental Models: Organisms/Strains		
AppNL-G-F	Saito et al., 2014	Available from the Saido lab.
C57BL/6 (control for for AppNL-G-F)	Janvier	C57BL/6Jrj
Software and Algorithms		
ImageJ	NIH	https://imagej.nih.gov/ij/
WGCNA	Zhang and Horvath, 2005	https://cran.r-project.org/web/packages/WGCNA/index.html
EdgeR	Robinson et al., 2010	https://bioconductor.org/packages/release/bioc/html/edgeR.html
GORilla	Eden et al., 2009	http://cbl-gorilla.cs.technion.ac.il/
ST pipeline	Navarro et al., 2017	https://github.com/SpatialTranscriptomicsResearch/st_pipeline

RESOURCE AVAILABILITY

Lead Contact

Further information and requests for reagents may be directed to, and will be fulfilled by the corresponding author Bart De Strooper (bart.destrooper@kuleuven.vib.be)

Materials Availability

This study did not generate new unique reagents.

Data and Code Availability

Raw and normalized count matrix of the Spatial Transcriptomics are available via the GEO database (GEO accession number GSE152506). Data and images of *in situ* sequencing are available at “Synapse.org” under the doi 10.7303/syn22153884: <https://repo-prod.prod.sagebase.org/repo/v1/doi/locate?id=syn22153884&type=ENTITY> <https://repo-prod.prod.sagebase.org/repo/v1/doi/locate?id=syn22153884&type=ENTITY> All data and analysis are available at “alzmap.org”: <https://www.alzmap.org/>

EXPERIMENTAL MODEL AND SUBJECT DETAILS

Mice

All animal experiments were conducted according to protocols approved by the local Ethical Committee of Laboratory Animals of the KU Leuven (governmental license LA1210591, ECD project number P056-2016) following governmental and EU guidelines.

App^{NL-G-F} knock-in (Saito et al., 2014) mice express Swedish (KM670/671NL), Beyreuther/Iberian (I716F), and Arctic (E693G) mutations in the *App* gene under the endogenous promoter on the C57BL/6J background. *App*^{NL-G-F} mice were in addition backcrossed for at least 2 generations with C57BL/6J mice in the De Strooper lab. It should be noticed that the APP locus in *App*^{NL-G-F} has been the result of a recombination event of a FVB generated transgene which means that an unknown number of FVB genes are in linkage disequilibrium with the *App*^{NL-G-F} transgene.

Male mice (*App*^{NL-G-F} KI and C57BL/6J controls) were sacrificed at 3.5 months (106 days), 6 months (average 183.5 days), 12 months (average, 367 days), or 18 months (average 551 days) of age, giving rise to 8 experimental groups (n = 2 per group for 3.5- and 18-months of age; n = 1 per group for 6- and 12-months of age; n = 12 for total): WT_03, WT_06, WT_12, WT_18, AD_03, AD_06, AD_12, AD_18. Following cervical dislocation, left and right hemispheres were embedded in cold OCT separately and snap-frozen in isopentane chilled with liquid nitrogen. Samples were stored at –80°C.

Human

The human brain tissues were obtained from the Netherlands Brain Bank (NBB), Netherlands Institute for Neuroscience, Amsterdam. Written informed consent was given by the donors for brain autopsy and for the use of material and clinical data for research purposes, in compliance with national ethical guidelines. Clinicopathological information of the donor including postmortem time, age and sex of the donor, pH as measure for agonal state, clinical information and recent drug history is recorded (Table S5). Neuro-pathological diagnosis of the A β deposition (stage A, B and C) and neurofibrillary tangles (stage I–VI) is provided (Table S5). We selected 3 individuals with clinically diagnosed as AD with pathology at the end stage (amyloid stage C and Braak stage V–VI) and 3 non-demented controls (NDC) with no or very little pathology. All individuals are female and matched for age (AD: average 76, NDC: average 75). Frozen brain blocks of superior frontal gyrus from 6 individuals were delivered on dry ice to the lab and stored at –80°C. Samples were cryosectioned to a thickness of 10 μ m using a CryoStar NX70 cryostat (ThermoFisher). Sectioned samples on glass slides were processed for *in situ* sequencing, and followed by immunostaining of A β .

METHOD DETAILS

Tissue collection for Spatial Transcriptomics

OCT-embedded hemispheres were cryosectioned coronally to a thickness of 10 μ m (bregma: –2.0 to –2.2) using a CryoStar NX70 cryostat (ThermoFisher). We layered tissue sections onto a spatially barcoded array to collect *in situ* 2D-RNaseq of Spatial Transcriptomics (Lot#10001, Spatial Transcriptomics, Stockholm, Sweden) or to a regular glass slide for immunohistochemistry. Each spatially barcoded array has 1007 TDs, with a diameter of 100 μ m and a center-to-center distance of 200 μ m, over an area of 6.2 mm by 6.6 mm. One coronal section normally covers the area of 500 to 600 spots on the array, each spot defining one TD. Each spot contains approximately 200 million barcoded reverse-transcription oligo(dT) primers allowing to get a global transcriptomic profile of a TD with a volume of 0.00008 mm³ ($\pi r^2 h$ with $r = 50 \mu$ m and $h = 10 \mu$ m). After cryosection, all sections were stored at –80°C before proceeding with experiments.

We collected one right and one left hemisphere for each experimental group at 3.5- and 18-months of age, and one right hemisphere for each experimental group at 6- and 12-months of age. We performed experiments on *App*^{NL-G-F} KI mice and C57BL/6J of the same age at the same time. RNA quality was checked by RNeasy Micro Kit (QIAGEN, Hilden, Germany) and Agilent 2100 Bio-analyzer with RNA nano chips (Agilent Technologies, Inc., Santa Clara, CA, USA). RIN values of the tissues were between 8.6 to 9.45. Details of sample quality is described in Table S1.

In situ 2D-RNaseq via Spatial Transcriptomics

Spatial Transcriptomics experiments were performed following the Library Preparation Manual (Spatial Transcriptomics, Stockholm, Sweden) (Stahl et al., 2016). Briefly, cryosectioned tissues were fixed on a spatially barcoded array by 3.7% formaldehyde solution at room temperature for 10 min, and stained by hematoxylin for 7 min, bluing buffer (Dako, CS702) for 2 min, and eosin for 20 s at room temperature. We acquired HE images by Zeiss Axio Scan.Z1 slidescanner (Carl Zeiss AG, Oberkochen, Germany). After imaging, tissues were immediately permeabilized by collagenase in HBSS-BSA buffer for 20 min and 0.1% pepsin in 0.1M HCl for 6 min at 37°C, and followed by *in situ* reverse transcription by adding cDNA synthesis master mix at 42°C for 18–20 hours to get the stable cDNA attached on the array. Tissue on the array was then removed by incubation with 2.5 mg/ml proteinase K in PDK buffer at 56°C for 1h with interval shaking (300 rpm, 15 s shake, 15 s rest), which left cDNA coupled to the arrayed oligonucleotides on the slide. We collected the cDNA probes by probe cleavage using 100U/ml USER enzyme in 1X second strand buffer with dNTP and BSA. Library preparation of the released cDNA probes was performed in the laboratory of our collaborator led by Prof. Joakim Lundeberg at KTH Royal Institute of Technology, Sweden, including second strand synthesis, *in vitro* transcription, adaptor ligation, second cDNA synthesis, qPCR quantification, and PCR amplification. The number of cycles used to amplify the final libraries is between 8–11 cycles. Library quality was checked on an Agilent BioAnalyser DNA High Sensitivity chip. We selected two out of six libraries per mouse with lower amplification cycles, better tissue morphology, higher RIN value, and similar length of cDNA to perform paired end sequencing on an Illumina NextSeq500 sequencer at the VIB Nucleomics Core (Leuven, Belgium). To determine the exact localization and quality of each of the 1007 TDs on the array, a fluorescent Cyanine-3 probe was hybridized to the remaining DNA capture probes and the

arrays were scanned at 548 nm by Zeiss Axio Scan.Z1 slide scanner (Carl Zeiss AG, Oberkochen, Germany). The image was used together with the HE-image to annotate the spatial localization of each TD using the Allan Brain atlas as reference.

Immunohistochemistry of Spatial Transcriptomics

Immunohistochemistry was performed on two extra sections adjacent to the section used for sequencing. After fixation in 4% ice-cold paraformaldehyde (PFA) for 20 min and a wash with PBS, we performed antigen retrieval by microwave boiling the tissue 3 times in 10 mM sodium citrate at pH 6.0 to expose antigenic sites. After cooling down to room temperature for 20 min, brain tissues were washed and blocked in TBS-buffer solution containing 0.5% Triton X-100 and 5% normal goat serum for 2h. The serum-blocked tissues were then stained with mouse Alexa Fluor 488 anti-A β_{1-16} antibody, 6E10 (803013, BioLegend) at 4°C overnight, and guinea pig anti-NeuN antibody (266004, Millipore) and rabbit anti-Gfap antibody (Z0334, DAKO) in blocking buffer at 4°C overnight. The immuno-stained tissues were then incubated with goat Alexa 568 anti-guinea pig IgG (H+L) antibody (A11075, Invitrogen) and goat Alexa 647 anti-rabbit IgG (H+L) antibody (A21245, Invitrogen) for 1.5 h at RT. After incubation with DAPI and mounting with mowiol, imaging was carried out on Zeiss Axio Scan.Z1 slidescanner (Carl Zeiss AG, Oberkochen, Germany) using a 20X objective. Volume images were acquired with 16-bit depth to allow a broad range of intensity values and rendered using Fiji (Schindelin et al., 2012).

In situ sequencing and immunostaining of mouse samples

OCT-embedded hemispheres of mice at 18-month of age were cryosectioned coronally into 14 μ m (bregma -2.0 to -2.2) and layered onto SuperFrost Plus glass slides (ThermoFisher) and further stored at -80°C before experiments. Samples were shipped on dry ice to CARTANA (Solna, Sweden) for tissue fixation, reverse transcription, probe ligation, rolling cycle amplification with reagents and according to the procedures supplied in the Neurokit (1010-01, CARTANA, Sweden), followed by fluorescence labeling, and sequencing by sequential images at 20X objective (Ke et al., 2013). Five probes were designed for each gene, except *Itgam*, which has 10 customized probes to increase the detection sensitivity. We included probes for 7 additional genes that do not belong to the PIG module but significantly react to the presence of amyloid plaques at 18-months of age in the ST analysis: *Cst7*, *Cd68*, *Ccl6*, *Prox1*, *Hcrt*, *Pmch*, and *C1ql2* (LFC: 1.91, 1.70, 1.69, -1.42 , -1.72 , -1.83 , and -2.01 , respectively). Probes with design issues (*H2-D1*, *Cd63-ps* and *RP23-269H21.1*) are removed and probes cross-reacted with their related genes are renamed (*C4a*, *C4b* as *C4*, *Serpina3n* as *Serpina3*, *Lyz2* as *Lyz*). To reduce lipofuscin autofluorescence, 1X TrueBlack (Biotium, Fremont, CA) was applied for 30 s before fluorescence labeling. The result table of the spatial coordinates of each molecule of 84 targets together with the reference DAPI image per sample were provided by CARTANA.

After *in situ* sequencing, samples were shipped back to the lead laboratory in Leuven for further immunostaining of amyloid plaques on the same tissue. Briefly, after removing coverslips, the brain tissues were washed and blocked in TBS-buffer solution containing 0.5% Triton X-100 and 5% normal goat serum for 2h. The serum-blocked tissues were then stained with mouse Alexa Fluor 488 anti-A β_{1-16} antibody, 6E10 (803013, BioLegend) at 4°C overnight. After immunostaining, sections were then incubated in 1X TrueBlack (Biotium, Fremont, CA) solution for 30 s to reduce lipofuscin autofluorescence. After staining with DAPI (Sigma-Aldrich) and mounting with FluorSave Reagent (Merck Millipore, Burlington, MA). Imaging was carried out on MÄRZHÄUSER SlideExpress 2 with 20X objective and Hamamatsu ORCA Flash4.0 camera. Volume images were acquired with 16-bit depth to allow for a broad range of intensity values and rendered using Fiji.

In situ sequencing and immunostaining of human samples

Human brain blocks were cryosectioned into 10 μ m and layered onto SuperFrost Plus glass slides (ThermoFisher) and further stored at -80°C before experiments. Samples were shipped on dry ice to CARTANA (Solna, Sweden) for *in situ* sequencing as mentioned above. In general, probe design is carried out by CARTANA (Solna, Sweden) using similar methods as in Qian et al. (2020) with modifications to enable higher specificity and constant performance. Five probes were designed for each gene, covering as many known isoforms of a gene as possible with minimal off-target detection. One exception is *CST3*, which has only two probes, due to high similarity between *CST1-5* sequences. The human genes included in the list are selected as mouse orthologs using either “one-to-one” or “one-to-many” homology type of the Ensemble 81 BioMart table. To reduce lipofuscin autofluorescence, 1X TrueBlack (Biotium, Fremont, CA) was applied for 30 s before fluorescence labeling. The result table of the spatial coordinates of each molecule together with the reference DAPI image per sample were provided by CARTANA.

After *in situ* sequencing, samples were shipped back to the lead laboratory in Leuven for further immunostaining of amyloid plaques on the same tissue. We found that the immunostaining protocol mentioned above for mouse amyloid plaques is not sufficient to detect amyloid plaques in human brain, so we included an antigen retrieval step to clearly detect and visualize A β deposits in AD patients. Briefly, after removing coverslips, protease K (1 $\mu\text{g}/\text{ml}$) was added onto brain tissues and incubated at 37°C for 30 mins. After washing twice with PBS, tissues were heated in 10 mM EDTA (pH 6.0 in H₂O) using microwave at 650 W to boil intermittently for 3 times and let it cool down at room temperature for 20 mins. After washing twice with PBS, we incubated the tissue with 100% formic acid for 3 mins at room temperature before processing for serum blocking. The serum-blocked tissues were stained with mouse purified anti-A β_{17-24} antibody, 4G8 (SIG-39220, BioLegend) at 4°C overnight, and followed by donkey anti mouse Alexa-647 (A31571, ThermoFisher) at room temperature for 1.5 hours. After immunostaining, sections were then incubated in 1X TrueBlack (Biotium, Fremont, CA) solution for 30 s to reduce lipofuscin autofluorescence. After staining with DAPI (Sigma-Aldrich) and mounting with FluorSave Reagent (Merck Millipore, Burlington, MA). Imaging was carried out on MÄRZHÄUSER SlideExpress 2 with 20X

objective and Hamamatsu ORCA Flash4.0 camera. Volume images were acquired with 16-bit depth to allow for a broad range of intensity values and rendered using Fiji.

Multiplexing RNAscope and immunohistochemistry

OCT-embedded hemispheres of 3 *App^{NL-G-F}* mice at 18-month of age were cryosectioned coronally into 14 μm (bregma -2.0 to -2.2) and layered onto SuperFrost Plus glass slides (ThermoFisher) and further stored at -80°C before experiments. RNAscope experiments were performed using the Manual Fluorescent Multiplex kit v1 (Advanced Cell Diagnostics, Newark, CA) following manufacturer's recommendations with minor adjustments. Briefly, after fixation and protease digestion, probe hybridization was carried out at 40°C for 2 h with the indicated probe sets. Probes were all from Advanced Cell Diagnostics: Mm-Cst7 (498711), Mm-Cd68-C3 (316611-C3), Mm-C4 (445161), Mm-C1qa (44221), Mm-Clu (427891), Mm-Syp-C3 (426521-C3), Mm-Mbp-C3 (451491-C3), Mm-Slc1a3-C3 (430781-C3), and Mm-Ilgam-C2 (311491-C2). After amplification steps to obtain the RNAscope signals, we immediately performed immunohistochemistry to acquire the immunofluorescence picture of amyloid-beta plaques in the tissues. Briefly, the sections were blocked for 1 hour at RT in PBS containing 0.3% Triton X-100 and 5% normal goat serum and immunostained with the anti- $\text{A}\beta_{1-16}$ primary antibody (6E10, BioLegend, San Diego, CA) at 4°C overnight and then with an Atto-488-conjugated goat anti-mouse secondary antibody (Sigma-Aldrich, Saint Louis, MO) at RT for 1 h. After immunostaining, sections were incubated in 1X TrueBlack (Biotium, Fremont, CA) solution for 30 s to reduce lipofuscin autofluorescence. After staining with DAPI (Sigma-Aldrich) and mounting with FluorSave Reagent (Merck Millipore, Burlington, MA), 6 different areas within hippocampus per coronal section were imaged via a Leica TCS SP8 X confocal microscope (Leica Microsystems, Wetzlar, Germany) using a 40X objective with 10 z stacks spacing of 1 μm per image.

To visualize the expression of 4 genes in the myelin module and $\text{A}\beta$ deposition across the full coronal section, we scaled up the imaging system. We performed the same processing to multiplex RNAscope and immunostaining as mentioned above by using 4 different probes: Mm-Mbp-C2 (451491-C2), Mm-Olig2-C3 (447091-C3), Mm-Cnp-C3 (472241-C3) and Mm-Plp1-C2 (428181-C2). After immunostaining, sections were imaged by MÄRZHÄUSER SlideExpress 2 with 20X objective and Hamamatsu ORCA Flash4.0 camera. Volume images were acquired with 16-bit depth to allow for a broad range of intensity values and rendered using Fiji.

QUANTIFICATION AND STATISTICAL ANALYSIS

Image analysis

Metadata of Spatial Transcriptomics

HE and Cy3-spot images were acquired from the middle ST sections. Fluorescent amyloid-beta, astrocyte, neuron, and nuclei images were acquired from the two adjacent sections stained by 6E10, anti-Gfap antibody, anti-NeuN antibody, and DAPI. Manually aligned HE and Cy3-spot images were used to bridge the transcriptomics picture with the immunostaining pictures. To de-barcode the spatial localization of each transcriptomic profile, we converted the pixel coordinates of the 1007 TDs on the Cy3-spot image into the theoretical coordinates described in the ID-file of the spatially barcoded array. To acquire the spatially corresponding amyloid and cellular information per TD, we manually aligned and transformed fluorescence images into the corresponding HE images. To annotate the anatomic brain regions, we manually aligned and transformed the reference atlas from Allen Brain Institute into the corresponding HE images. More details of the reference atlas for each sample are described in [Table S1](#). Image alignment was processed using the Fiji plugin "Landmark correspondences" ([Legland et al., 2016](#)) and the precision of all aligned images were checked before analysis.

We developed a Fiji groovy script package to automate the image processing and analysis. Quality of the image has been checked before computation. We annotated the unreliable areas (e.g., damaged tissue, out of focus, or dirt on the image) by manual assignment of region of interest (ROI) by Fiji. For each TD, the package computed the percentage of damaged area, coverage area of tissue, coverage area of Cy3-detectable spot, and the coverage area of individual brain region according to the Allen Brain atlas images. Spots with coverage area of tissue $> 90\%$, damaged area of tissue $< 30\%$, and coverage area of Cy3-detectable spot $> 90\%$ are filtered. This results in 500-600 useful TDs for each sample.

To measure the immunostainings, we computed 5 parameters for the $\text{A}\beta$, the Gfap, the NeuN and the DAPI staining within each TD: (1) mean pixel intensity, (2) median pixel intensity, (3) sum of pixel intensity, (4) standard deviation of pixel intensity, and (5) percentage of area of the computed positive signals per TD.

Quantification of immunostainings

To assign a single measure to a TD for each of the immunostainings, we computed 5 statistics for each TD and staining ($\text{A}\beta$, Gfap, NeuN and DAPI): (1) mean pixel intensity, (2) median pixel intensity, (3) sum of pixel intensity, (4) standard deviation of pixel intensity, and (5) percentage of area of the computed positive signals per TD. To select the most representative statistics, a group of 8 experts were employed in a random ranking approach. In this exercise, two images of random TDs (showing the same staining) were shown side by side, and we asked the experts to identify the TD image which, according to their best estimate, contains the highest amount of stained material. For each staining we scored a large number of pairs ($\text{A}\beta$: 1672, DAPI: 1685, NeuN: 1464, Gfap: 2271). Subsequently, we calculated for every scored pair and for each calculated parameter, the difference between the two TDs. We then used the Mann Whitney U test (MWU, p value) to identify which parameter has the best power to distinguish between the two TDs, and, which parameter is most often in concordance with the expert. Based on this approach, we picked the percentage of

area of the computed positive signals for Gfap (80.14% correct, MWU $p = 10^{-297}$), DAPI (79.35% correct, MWU $p = 10^{-167}$) and NeuN (72.13% correct, MWU $p = 10^{-121}$). Remarkably, the standard deviation of pixel intensity worked best for the A β (66.51% correct, MWU $p = 10^{-92}$). We experimented with normalization per slide, but this did not improve the predictive power, so we proceeded without normalization. The final score taken per staining/TD is the mean of the corresponding spot in the two adjacent slides.

Metadata of *in situ* sequencing

We manually aligned the amyloid immunostaining with the DAPI reference. As *in situ* sequencing and immunostaining were carried out on the same tissue, the precision of alignment is very high and has been checked before analysis. We converted the A β -positive signals into binary masks by using a histogram-derived threshold method, Triangle, in Image-J. The ROI of the plaque cellular niche (ring 1) is based on the area mask with boundary expansion by 10 μm . We compute 5 co-centroid circles (donuts) from the ROI of ring1 in the plaque cellular niche to the ROI of ring5 far from plaque with 18.2 μm (same parameter as RNAscope quantification below) extension per ring without overlap between plaques. The assignment of the spatial distance to plaque per fluorescence punctum is based on the spatial coordinates per punctum provided by CARTANA. The metadata generated by this image analysis was further applied in the data analysis of the *in situ* sequencing experiment. We used QuPath to overlay the spatial images of multiple targets, immunostainings, DAPI staining, and ROIs of cells and plaques, and to generate the representative images shown in the figures (Bankhead et al., 2017). This procedure is the same for both mouse and human samples.

RNAscope quantification

Three male AppNL-G-F mice per experimental condition were used for quantification. For each mouse, images of the hippocampus acquired by Leica TCS SP8 X confocal microscope were analyzed. We took the maximum intensity projection of 10 z stacks and used the NIS-elements software 5.20.01 (Nikon Instruments Europe BV.) to detect nuclei, microglia, astrocytes, neurons, oligodendrocytes, and plaques using a custom-made GA3 protocol. To get the single cell resolution, the ROI of a segmented single nucleus (based on DAPI staining) was expanded by 10 μm . With each ROI per cell, we computed the number of RNAscope puncta per gene. Microglia, astrocytes, neurons, and oligodendrocytes were identified by RNAscope puncta from the Itgam, Slc1a3, Syp, and Mbp probes, respectively. All parameters were kept constant between images to allow unbiased detection. Around each plaque, five concentric circles were drawn. The ROI of the plaques (ring 1) is based on the area mask of 6E10 staining with boundary expansion by 10 μm . We compute 5 co-centroid circles (donuts) from the ROI of ring 1 in the plaques to the ROI of ring 5 far from plaque with 18.2 μm (65 pixel) extension per ring without overlap between plaques. For each ring we counted microglia, astrocytes, neurons, and oligodendrocytes, and for each cell we measured the intensity of the signal (e.g., Cst7, Cd68, C1qa, C4). To quantify the degree of change around amyloid plaques, we first log transformed the target intensity per cell, and classified their expression level per cell to the distance to amyloid plaques (ring). To get the expression profiles of Mbp, Plp1, Cnp and Olig2 over all coronal sections, the images of full coronal section of each mouse acquired by the microscope “Nikon NiE-MÄRZHÄUSER SlideExpress 2” were analyzed. We developed a custom-made GA3 protocol based on the NIS-elements software 5.20.01 to compute the number of fluorescence puncta of each gene per ring and the total area of each ring in a full coronal section.

Sequencing Data Analysis

Generation of raw counts, cpm counts

Sequencing data were pre-processed with the ST pipeline (Navarro et al., 2017), which filtered low quality bases, mapped against the mouse genome (Ensembl 88), and generated a count matrix. The count matrix was further filtered by removing spots with tissue coverage less than 30% in the HE image. The EdgeR “cpm” function was used for library size normalization and the output log-cpm matrix was used for the rest of the analyses.

Differential expression analysis

DE analysis was conducted by fitting two separate generalized linear models (GLM) using A β intensity and genotype information respectively. Each GLM model was tested for differential expression by using EdgeR quasi-likelihood F-test which accounts for the uncertainty in dispersion estimation at the age of 3 months and 18 months, separately. The A β model represents transcriptional changes under A β exposure, which models the log transformed A β index as a continuous variable, and its LFC indicates the changes in gene expression per unit change in A β index. For a more straightforward interpretation, we multiply all LFC by a constant 4.59 (the difference between the maximum observed A β and the minimum observed A β index across the database). The corrected LFC represents the amount of changes in gene expression from the minimum to the maximum observed A β load, and is used throughout the paper. The genotype model assesses transcriptional changes between WT and TG mice.

WGCNA

WGCNA package in R (Zhang and Horvath, 2005) was used to build signed co-expression networks. The set of genes with the highest 50% standard deviation was selected using the “varFilter” package from the Bioconductor (Huber et al., 2015). Soft power 14 was chosen by WGCNA’s “pickSoftThreshold” function to calculate the adjacency matrix, and the module identification was performed by the “cutreeDynamic” function by selecting deepSplit = 4. The adjacency matrix is calculated using the “adjacency.fromsimilarity” function using the signed network and soft thresholding power 14. The mean of the connectivity score of a given module is calculated by first taking the row sum of the adjacency matrix as the intra modular connectivity score per gene, and then the average of the intra modular connective score of all genes in the given module was calculated.

Selection of ARM/DAM genes

The 61 ARM/DAM markers are selected from the overlaps of top 120 ARM (Sala Frigerio et al., 2019) and top 120 DAM (Keren-Shaul et al., 2017) genes sorted by FDR.

Functional Enrichment

Functional annotation of the DE analysis was performed by GOrilla using the “Single ranked list of genes” model. For each DE analysis, two ranks are generated using LFCs, one from the most negative to most positive, and vice versa. The software will search for GO terms that are enriched in the top of the list compared to the rest of the list using the mHG statistics. Total of 8 GOrilla analyses were performed for each age group (3 months and 8 months) and Genotype and Plaque, respectively. Bonferroni correction was performed on all Gorilla analyses based on the total number of comparisons (21825 GO terms * 8 ranks = 174600).

Functional annotation of each module was performed by GOrilla using the “Two unranked lists of genes” model. Each module is used as the target list and the total of 36715 genes expressed in our dataset were used as the background set. The software searches for GO terms that are enriched in the target set compared to the background set using the standard Hypergeometric statistics.

To merge similar GO terms into cluster, we first generated a similarity matrix between all significantly enriched GO terms based on the number of the genes overlapping between two GO terms. Next, we performed hierarchical clustering using the complete linkage method, with tree height 3.3 which grouped all significant GO terms into 12 functionally overlapping clusters.

Binomial test of gene enrichment in the cellular niche (ring 1) of the amyloid plaque

To test if a gene of interest is significantly enriched in ring1, we used two-sided binomial test to compare the fraction of puncta of the corresponding gene in ring1 relative to the total number of puncta of the same gene in all rings (q) against the expected proportion (a), which is the proportion of the area of ring1 to the area of all rings. The logged odds ratio is then calculated as formula 1. All p values are multiple corrected using Bonferroni method.

$$\text{Log}_2(\text{oddsratio}) = \log_2 \frac{q(1-q)}{a(1-a)} \quad (\text{formula 1})$$

Cellular signature of the in situ sequencing data

Conventional cell segmentation relies on determining artificial borders around DAPI nuclei staining, and is prone to errors due to varying cell shape. On top of that the sparsity (low sensitivity) of the ISS data yielded segmented cells with very low puncta counts per cell (mean = 10.7 among the cells with at least one punctum). These biases make it difficult to reliably identify the cell identity. Therefore, we developed a segmentation-independent method to assign a candidate cell type to individual punctum by its proximal markers (Table S6). Calculation performed directly on all puncta from a full section instead of puncta counts per cell, increases statistical power, and proved to be much more robust (Figure S7).

The first step is to transform the distances between the investigated punctum (d_p) and each cell type marker punctum p into distance scores (V_p) using the following logistic function (Figure S7A):

$$V_p = \frac{1}{1 + e^{s(d_p - r)}} \quad (\text{formula 2})$$

Parameters are: d_p - the distance to a cell type marker punctum (in pixels); r - the distance at which $V_p = 0.5$ - an indication of the investigation radius of the punctum (mouse: $r = 15$ pixels = 4.875 μm , human: $r = 30$ pixels = 9.75 μm) (Figure S7B); and s - a measure of the steepness of the logistic curve ($s = 0.9$) (Figure S7C). Note, considering r as a proxy for cell size, the maximum d_p (307 pixels $\approx 100 \mu\text{m}$) is well above reasonable values for r . With $d_p > r$, V_p quickly approaches zero, and hence, puncta with a $d_p > r$ do not count toward cell type assignment.

The next step is to calculate a cell type score (S_{ct}) for each punctum by combining the distance scores (V_p), per cell type, into a cell type score (S_{ct}) of the investigated punctum:

$$S_{ct} = \frac{\sum_{p \in ct} V_p}{\max(k=2, \sum_p V_p)} \quad (\text{formula 3})$$

Where $\sum_{p \in ct} V_p$ is the sum of all distance scores (V_p) belonging to a particular cell type (ct). $\sum_p V_p$ is the sum of V_p for all cell type markers. To prevent the assignment of a punctum based on a single marker gene in very sparse regions we take $\max(k, \sum_p V_p)$ with $k = 2$.

Note that:

$$S_{neuron} + S_{oligodendrocyte} + S_{microglia} + S_{astrocyte} < 1 \quad (\text{formula 4})$$

The last step is to assign a cell type to a punctum based on a cutoff (0.75) (Figure S7D). By choosing a cutoff > 0.5 , we ensure only one cell type can be assigned to a punctum. By taking $k = 2$ (in formula 3), we enforce that at least two marker genes need to be close to the punctum in question for a cell type to be assigned.

We tested how different parameters affect cell type assignment in mouse and in human prior deciding on the combination of parameters used and reported above (Figure S7). The results are consistent when using different values for parameters, indicating the robustness of the method.

Finally, for both the mouse and human ISS analysis the cell type assignment incorporates all reported marker genes into the cell type call for each punctum. Each punctum is assigned to only one (or no) cell type based on the presence of multiple markers for that cell type, as well as the absence of markers for other cell types.

To investigate the enrichment of gene puncta in a particular cell type, we performed two-sided Fisher's exact tests in three groups (WT/NDC; *App*^{NL-G-F}/AD; and *App*^{NL-G-F}/AD in ring1) separately by comparing puncta of each gene in each cell type, against all puncta of that gene and all puncta of that cell type. P values are multiple corrected using FDR_BH across all genes of interest.

ADDITIONAL RESOURCES

We developed an online software to access all data and analysis at "alzmap.org": <https://www.alzmap.org/>

Supplemental Figures

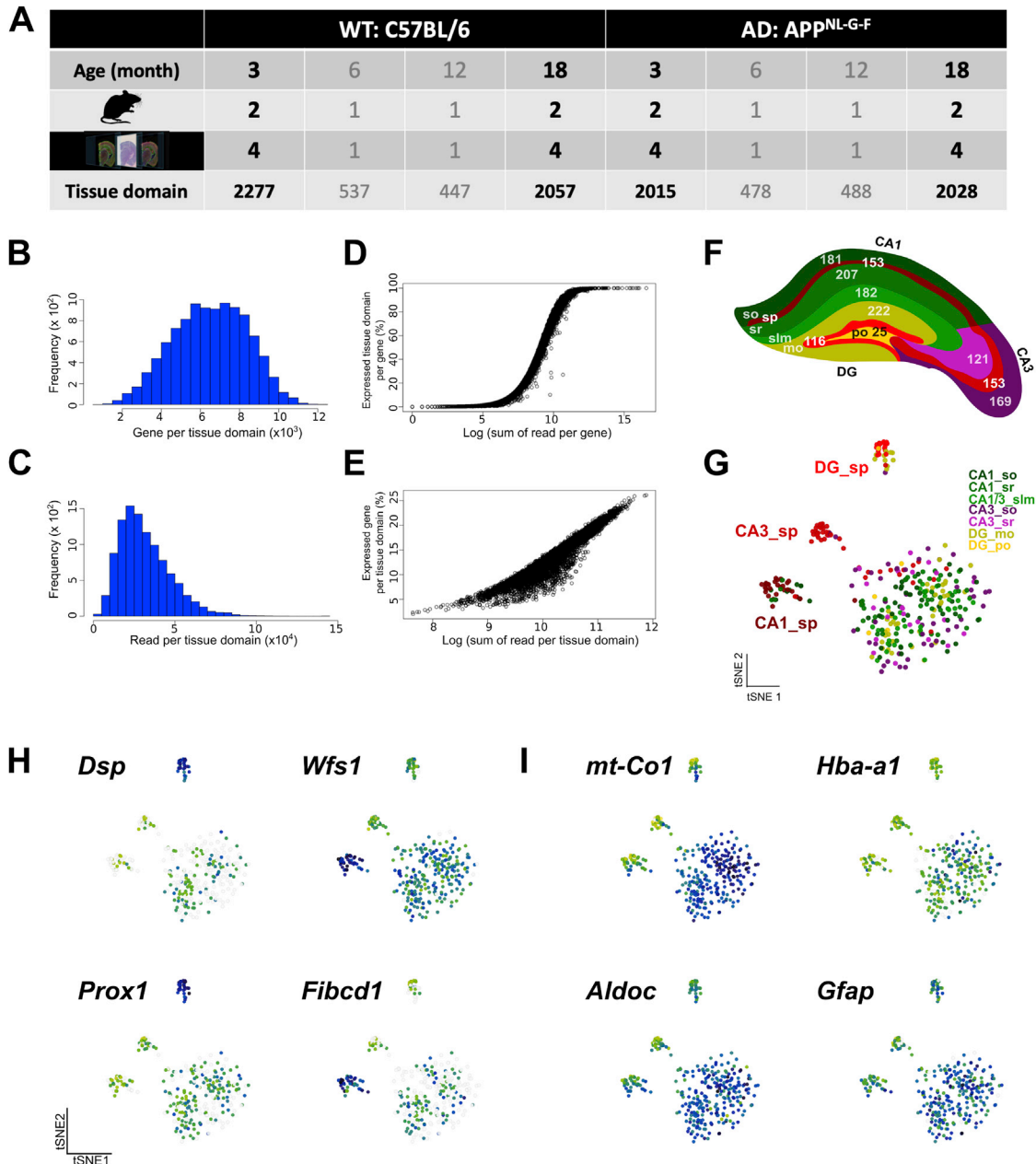


Figure S1. Experimental Setup and Data Quality, Related to Figure 1

(A) Summary of sample size, number of mice, number of ST experiments and total number of TDs passing quality control per age and genotype group.

(B and C) The distribution of the number of genes or reads per TDs.

(D) Each dot represents a gene, and in total 46454 genes were detected in the full database. The scatterplot shows the distribution of total number of reads per gene (x axis) and the percentage of TDs expressing each gene (y axis). Among 46454 genes, 1970 genes have only one copy; 25665 genes were lowly expressed (LogRead < 5); and 40 genes were highly expressed (LogRead > 13) such as *Plp1*, *Mbp*, *Sez6*, and *Apoe*.

(E) Each dot represents a transcriptomic profile of a tissue domain (TD), in total 10327 TDs are available. The scatterplot shows the distribution of total number of reads per TD (x axis) and the percentage of expressing genes per TD (y axis).

(F) Total number of TDs per region in hippocampus.

(G) t-distributed Stochastic Neighbor Embedding (t-SNE) plot visualizing 355 transcriptomic profiles in WT hippocampus at 3-months of age. TDs cluster according to somatic layers CA1, CA3, and DG.

(legend continued on next page)

(H and I) The same t-SNE plot as panel G, but TDs are colored according to gene expression of landmark genes in somatic layers (H) or metabolic genes in dendritic layers (I). As shown in panel H, *Dsp* and *Prox1* were localized in the granule cell layer of Dentate Gyrus (DG_sp), while *Fibcd1* and *Wfs1* were localized in the pyramidal layer of CA1 (CA1_sp). In addition, we also found enrichment of *mt-Co1* (cytochrome c oxidase), *Aldoc* (aldolase c), *Hba-a1* (hemoglobin subunit A1), and *Gfap* (glial fibrillary acidic protein) in the dendritic layer of hippocampus in panel I. This observation is in line with previous reports that the dendritic layer serves as the metabolic center of the hippocampus, containing the most microvessels, astroglial and highest activity of metabolic enzymes, including *mt-Co1* or *Aldoc* encoding proteins (Borowsky and Collins, 1989).

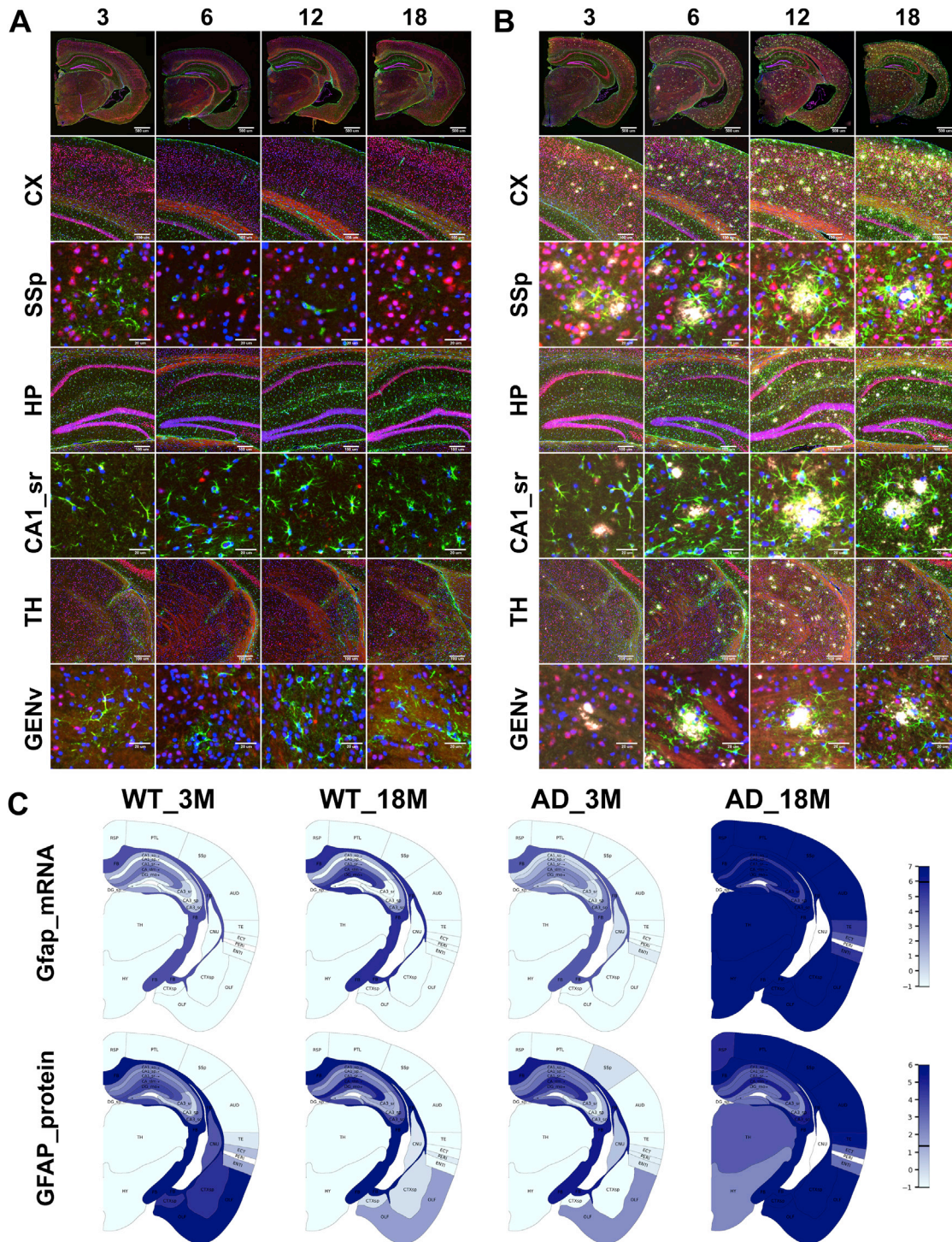


Figure S2. Amyloid Deposition and Astrogliosis, Related to Figure 2

(A and B) Immunofluorescent staining of amyloid plaques (mAb 6E10, white), astrocytes (Gfap, green), neurons (NeuN, red), and nuclei (DAPI, blue) in coronal sections of C57BL/6 (A) and *APP^{NL-G-F}* (B) brain at the indicated age. Selective zoom-ins of neocortex, hippocampus, and thalamus are displayed. Scale bar: 500 μ m in full coronal section, 100 μ m or 20 μ m in the zoom-ins. CX_SSp: primary somatosensory area of cortex, HP_CA1_sr: field CA1, stratum radiatum of hippocampus; TH_GENv: Geniculate group, ventral thalamus.

(C) Regional plots showing the expression levels of GFAP protein and *Gfap* mRNA at the indicated region, age and genotype. Expression levels are indicated by the mean z-score of GFAP protein or *Gfap* mRNA in the TDs from each group.

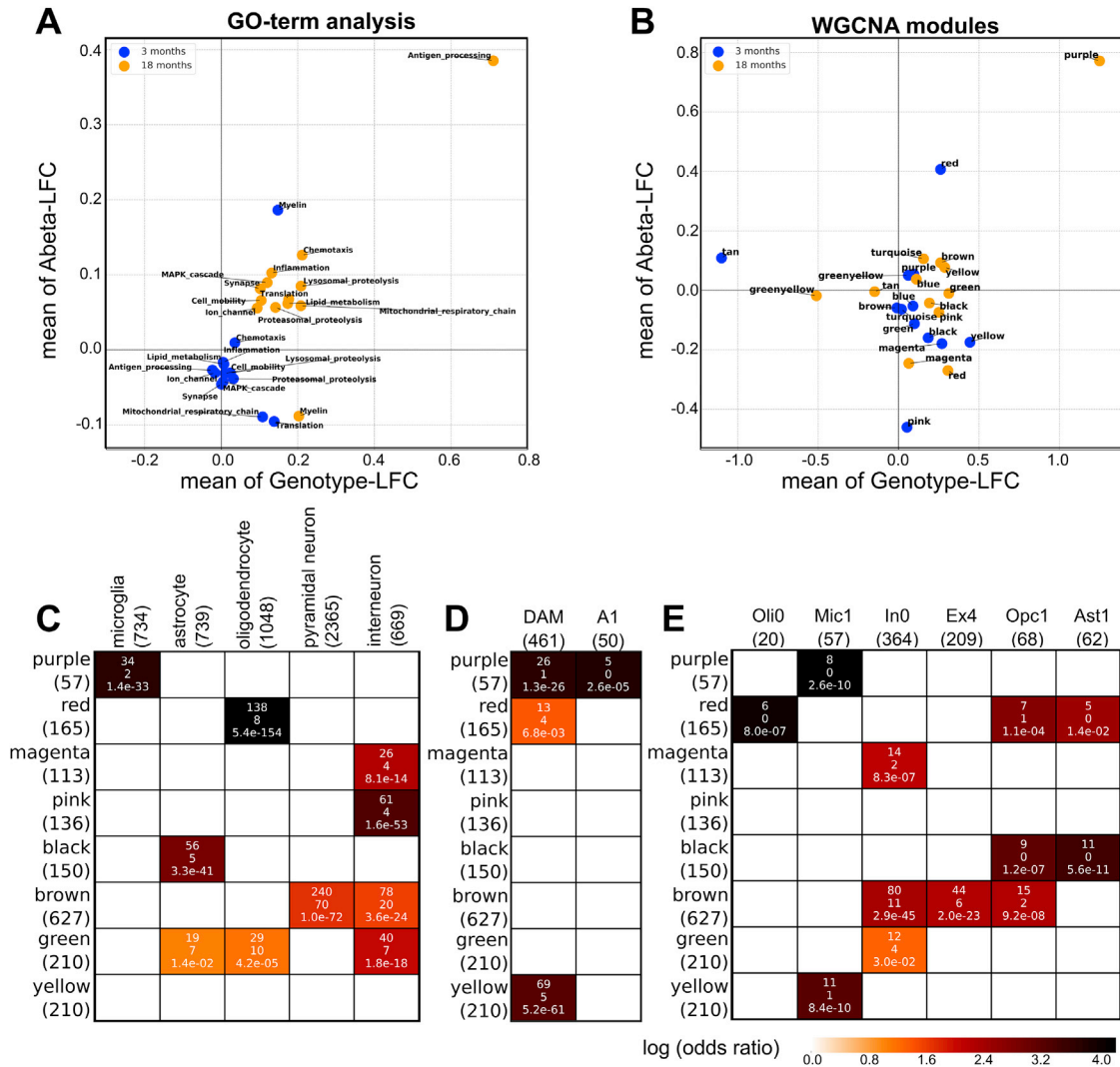


Figure S3. Gene Ontology Analysis and Co-expression Networks Defined by WGCNA, Related to Figures 3 and 6

(A and B) Summary of the differentially expressed genes in function of A β exposure or genotype analyzed by GORilla (A) and WGCNA (B). Panel A shows the significantly changed 13 super GO-categories, while panel B shows the alteration of 12 WGCNA-identified modules in both the A β - and genotype-axis at 3-months (blue) and 18-months (orange) of age. These A β -disease interaction plots take the average of LFC of genes in each GO-category (A) and in each module (B) of the indicated axis.

(C–E) Cellular signatures of each WGCNA module deduced from different published single-cell transcriptomic datasets as indicated below in mouse (C and D) or in human (E). The plots show significant overlaps between the identified WGCNA modules and a selection of publicly available gene sets as indicated below. The overlap is tested by Fisher’s exact tests, $p < 0.05$ FDR-BH corrected. The tan (34 genes) and green-yellow (39 genes) modules do not overlap with any gene sets, while the blue (3202 genes) and turquoise (4592 genes) modules act as dump modules and overlap with most of gene sets, thus not shown in the plots. We indicate the number of markers per gene set between brackets. Each block shows the number of genes shared (top), the number of genes expected to be shared by chance (middle) and the corrected p value (bottom). (C) The association of each module with mouse cellular populations from wild-type (CD-1) mice (Zeisel et al., 2015). (D) The association of each module with disease-associated glial populations identified in mouse models: disease-associated microglia (DAM) (Keren-Shaul et al., 2017) and inflammatory astrocytes (A1) (Liddelow et al., 2017). (E) The association of each module with AD-associated cellular subpopulations identified from 48 human individuals (Mathys et al., 2019): AD-associated oligodendrocyte (Oli0), microglia (Mic1), interneuron (In0), excitatory neuron (Ex4), oligodendrocyte precursor cell (Opc1), and astrocyte (Ast1). These results show a strong enrichment of the PIG module with human AD-associated microglia orthologs (Mic1). We do not find association of the PIGs with marker genes of populations with no AD-pathology traits.

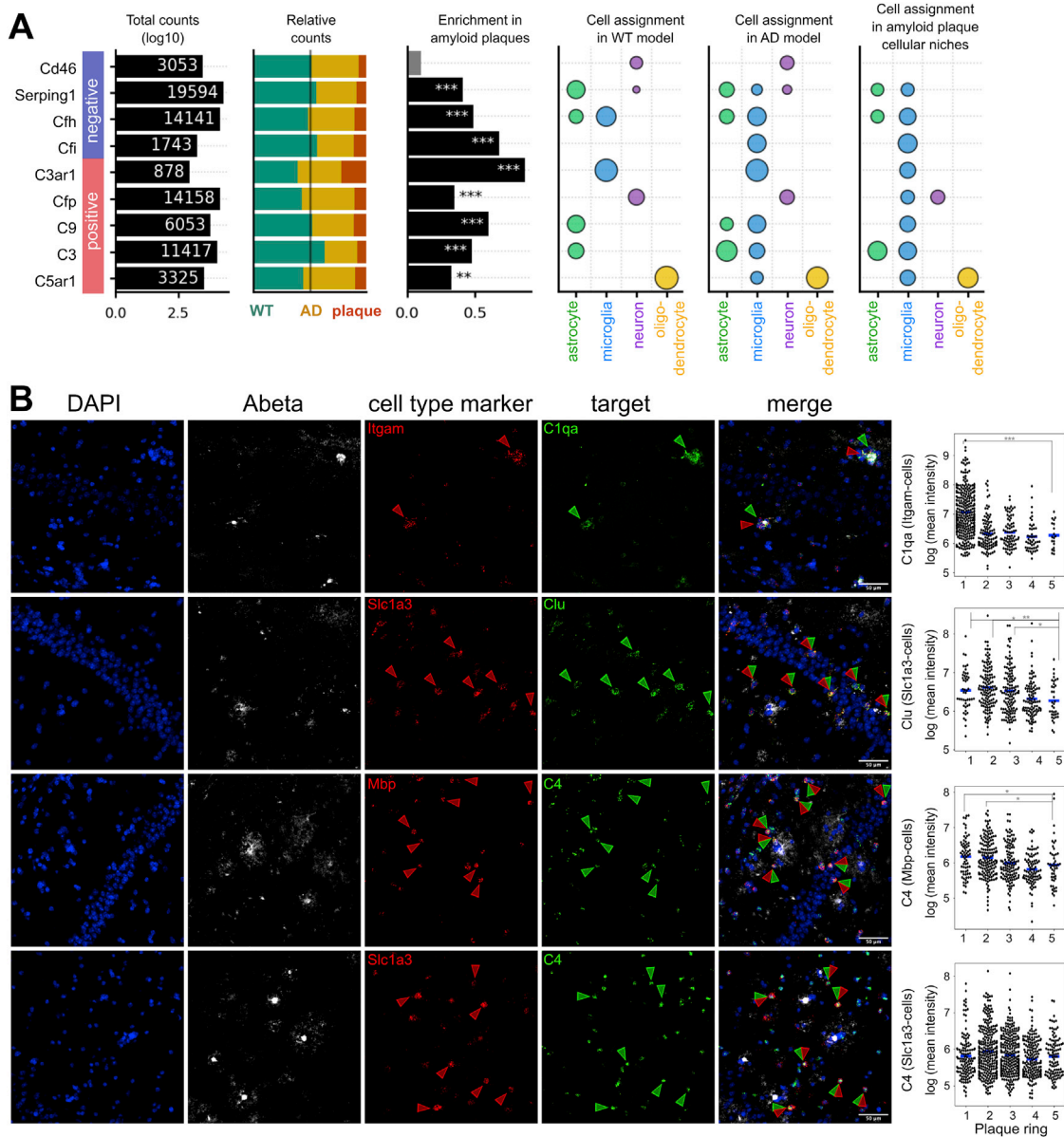


Figure S4. Microglia, Astrocytes, and Oligodendrocytes Are Involved in Activation of the Complement Cascade around Amyloid Plaques, Related to Figures 3 and 4

(A) Cellular signatures of the complement components as measured by ISS. “Total counts” shows the total number of puncta of each gene detected across 4 coronal sections from 2 genotypes. “Relative counts” shows the proportion of puncta detected in WT, in *App^{NL-G-F}* and around plaques, respectively. “Enrichment in amyloid plaques” displays the log2 odds ratio of gene puncta enriched in plaques using binominal test, with negative value indicating depletion. “Cell assignment” in WT, *App^{NL-G-F}* or plaques display the enrichment (log2 odds ratio) of each gene in a particular cell type using Fisher’s exact test (Benjamini-Hochberg corrected p value < 0.05). The size of balls is proportional to logged odds ratio.

(B) Combined RNAscope and immunofluorescence analysis of complement components (*C1qa*, *C4* or *Clu* in green) expression by microglia (*Itgam*, red), oligodendrocytes (*Mbp*, red), astrocytes (*Slc1a3*, red), and neurons (*Syp*, red) in the vicinity of amyloid plaques (6E10, white) in the hippocampus of *App^{NL-G-F}* mice at 18-month of age. Nuclei are blue (DAPI). Scale bar: 25 μ m.

(C) Quantification of *C1qa*, *C4* and *Clu* staining intensity per cell, classified based on cell type and distance from each plaque. Measurements were made from > 2900 single cells for each condition from 3 *App^{NL-G-F}* mice. Expression of *C1qa* in microglia, of *C4* in oligodendrocytes, and *Clu* in astrocytes were increased in the plaque cellular niches. *p < 0.05, **p < 0.005, ***p < 0.0005, Mann Whitney U test compared to the 5th ring p values corrected by Benjamini-Hochberg procedure.

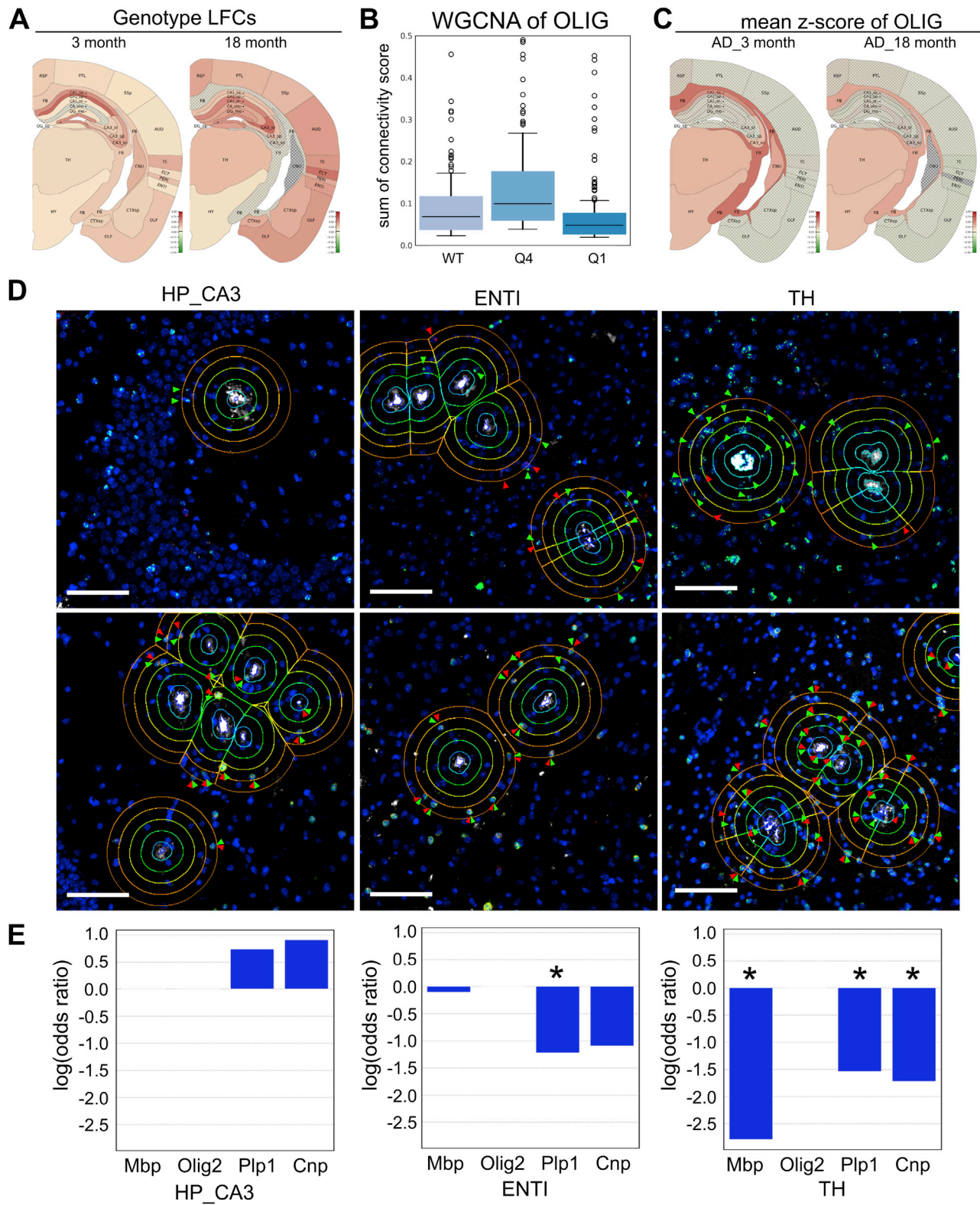


Figure S5. Spatial and Temporal Distribution of the OLIG Module, Related to Figure 6

(A) Average of LFCs of 165 genes in the OLIG module per region in *App^{NL-G-F}* versus WT at 3 and 18 months of age (region with mesh: non-significant LFCs, $p > 0.0001$).

(legend continued on next page)

(B) Sum of the connectivity score of gene pairs in the OLIG module in all TDs in WT, in TDs with low A β exposure (Q4), and in TDs with high A β exposure (Q1) in *App^{NL-G-F}*. The strength of co-expression of the OLIG module is highest in TDs with low A β exposure (Q4). * $p < 0.0001$, Mann Whitney U test.

(C) The OLIG expression (mean z-score of the 165 genes) per region in the *App^{NL-G-F}* mice at 3 and 18 months of age (region with mesh: $p > 0.0001$).

(D and E) Combined RNAscope and immunofluorescence analysis of amyloid plaques (anti-A β_{1-16} antibody, clone 6E10, white) and *Mbp*, *Olig2*, *Plp1* and *Cnp* transcripts (red and green, arrowhead) in hippocampal CA3 area (HP_CA3), entorhinal cortex (ENTI), or thalamus (TH) of *App^{NL-G-F}* mice at 3-months of age. Nuclei are blue (DAPI). Scale bar: 100 μ m. (E) The y axis shows the logged odds ratio of each transcript in plaques (ring1) in the indicated brain regions. * $p < 0.05$, FDR-BH p value correction.

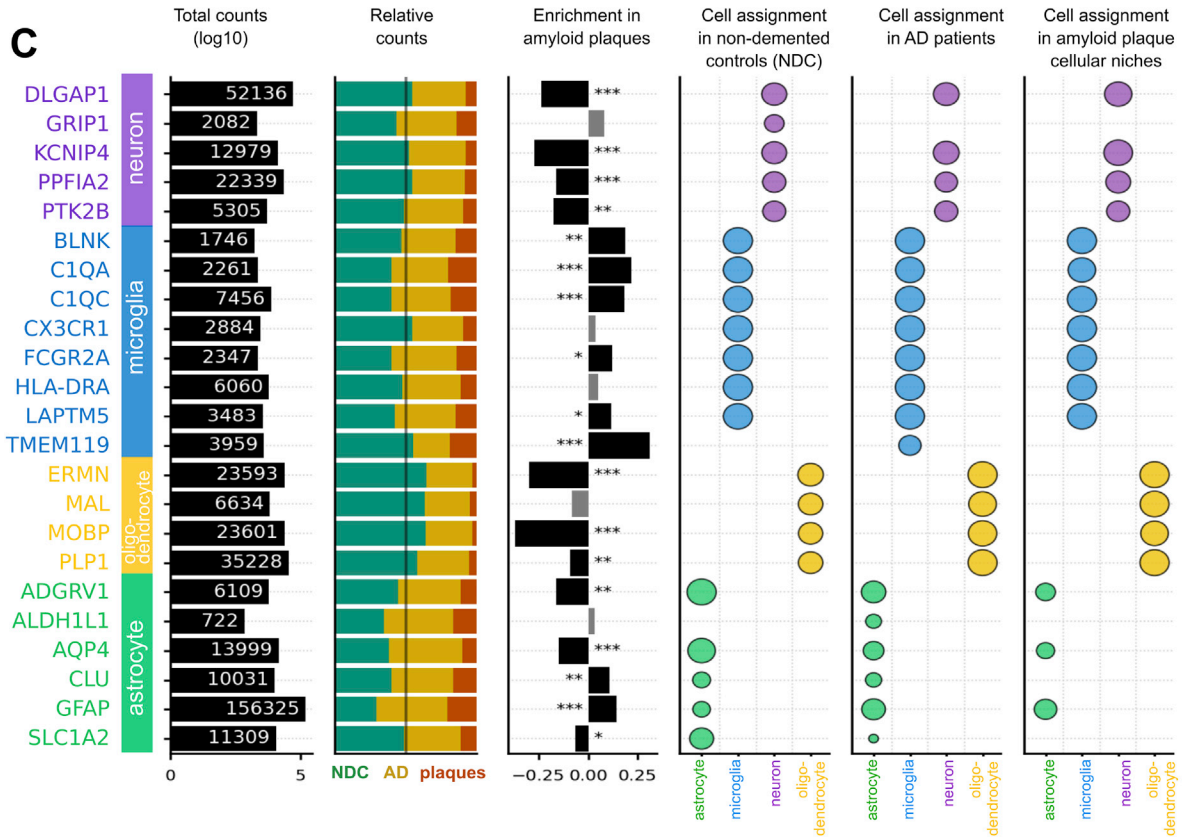
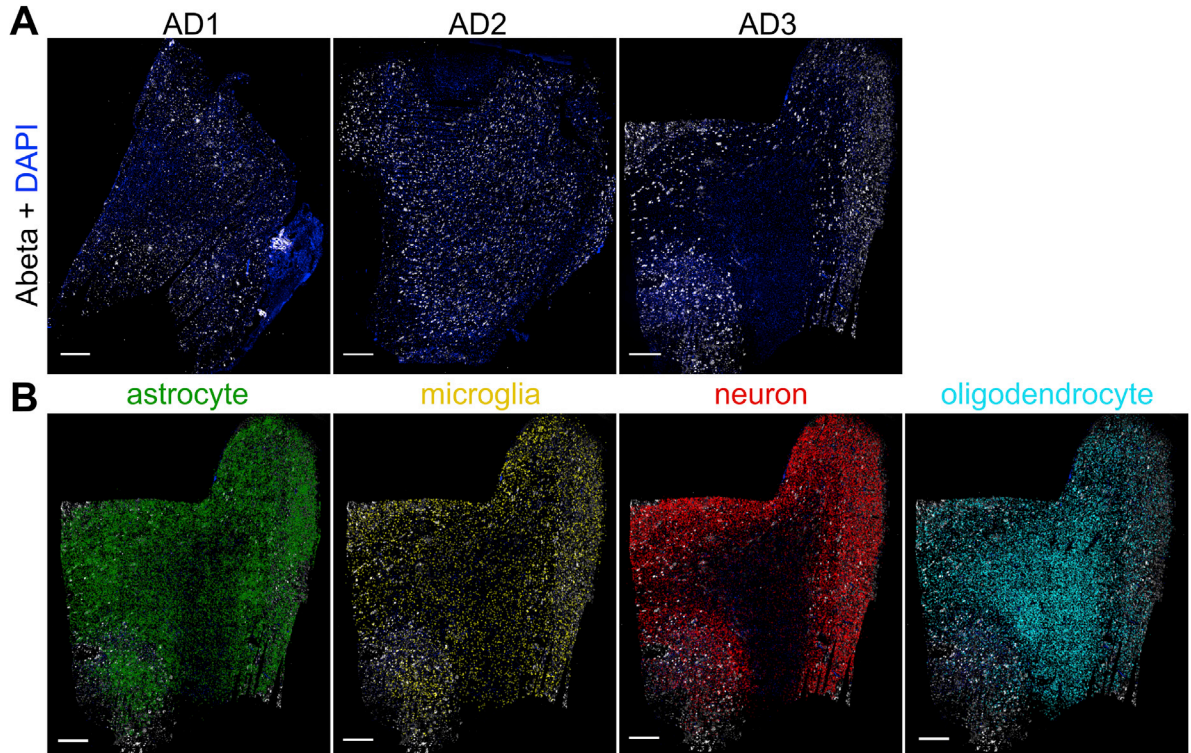


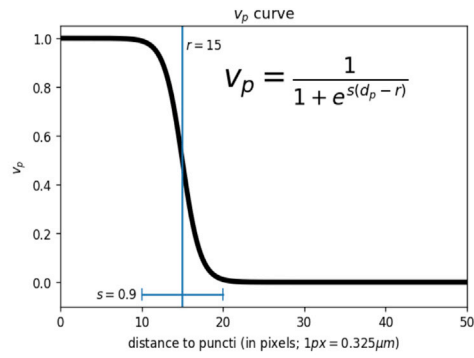
Figure S6. Amyloid Plaque Deposition and Cellular Distribution in Human Brains, Related to Figure 7

(A) Distribution of amyloid plaques (6E10, white) and nuclei (DAPI, blue) in the superior frontal gyrus of each AD individual.

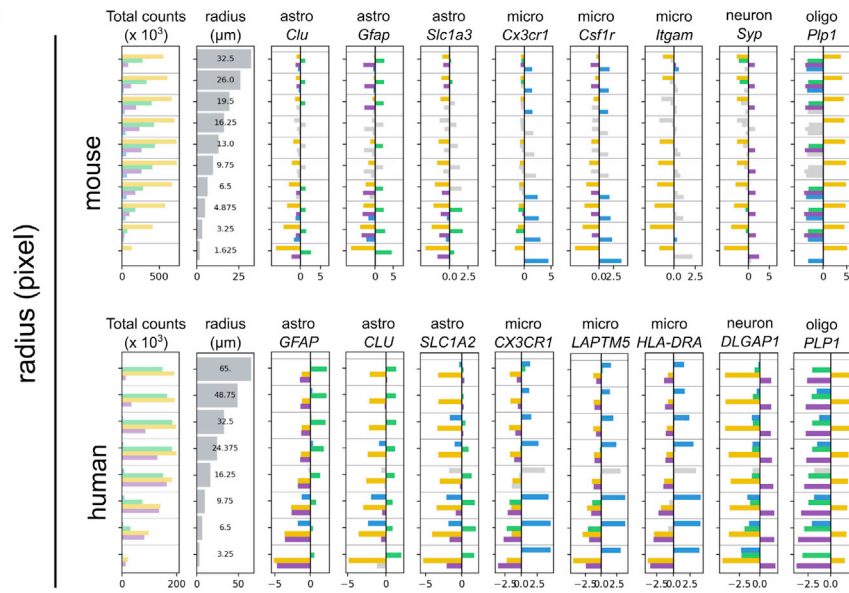
(B) Distribution of amyloid plaques (6E10, white) and cell type markers including green astroglial (*ADGRV1*, *AQP4*, *GFAP*, *ALDH1L1*, *SLC1A2* and *CLU*), yellow microglial (*CX3XR1*, *C1QA*, *BLNK*, *LAPTM5*, *HLA-DRA*, *FCGR2A*, *C1QC* and *TMEM119*), red neuronal (*DLGAP1*, *PPFIA2*, *KCNIP4*, *PTK2B* and *GRIP1*), and cyan oligodendroglial transcripts (*MAL*, *MOBP*, *PLP1* and *ERMN*). Scale bar: 1000 μm .

(C) Cellular signatures of the selected markers. The column "Total counts" shows the total number of puncta of each gene detected across 6 individuals. The "Relative counts" shows the proportion of puncta detected in non-demented controls (NDC), AD patients and plaques of AD, respectively. "Cell assignment" in NDC, AD, and plaques of AD columns display the enrichment (logged odds ratio) of each gene in a particular cell type using Fisher's exact test (FDR corrected p value < 0.05). The size of balls is proportional to log₂ odds ratio.

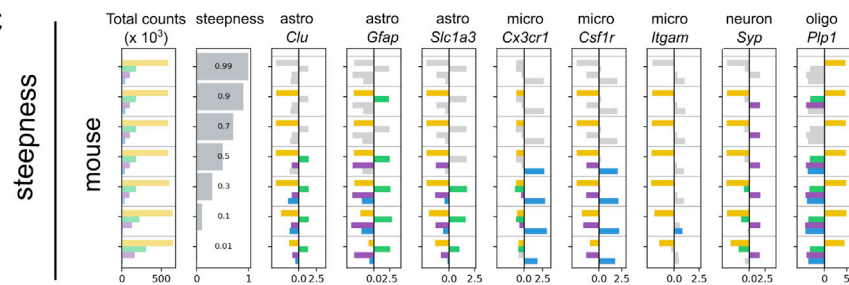
A



B



C



D

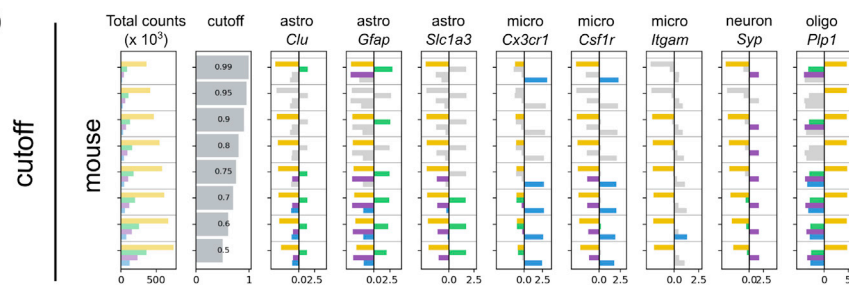


Figure S7. A Segmentation-Independent Method to Assign a Cell Type to an Individual Punctum, Related to Figures 4 and 7

(A) A logistic curve is used to determine distance measure (V_p) from the distance between a punctum and a marker gene punctum (d_p), here with $r = 15$ pixels as the sigmoid midpoint (blue line), and $s = 0.9$ as the steepness of the curve. We test how different parameters affect cell type assignment in mouse and human below: r for mouse or human (B) and s for both mouse and human (C). The first column shows the total number of puncta (in thousands) assigned to a cell type: oligodendrocyte (orange), astrocyte (green), neuron (purple) and microglia (blue). The second column shows the value of the parameter under investigation. The remaining columns each represents one cell type marker gene, showing the odds ratio of enrichment in a cell type. A positive odds ratio represents enrichment, whereas a negative odds ratio depletion. The column header indicates both the gene name, and the cell type for which this gene is considered a marker. (B) The effect of radius is investigated in both mouse (top) and human (bottom) plot. Overall, we see a strong enrichment of all cell type markers in the corresponding cell types, and depletion in other cell types. Increasing the radius in general increases the total number of puncta assigned to a cell type, however it does deteriorate the odds ratios. In the end, we have chosen $r = 15$ pixels (5 μm) for mouse and $r = 30$ pixels (10 μm) for human, which are reasonable approximations of the average cell size in each species. (C) We test how the steepness (s) of the curve affects cell type assignment. The result shows that the steepness has little impact on the cell type enrichment analysis, we settled on 0.9 for the downstream analysis for both mouse and human. (D) To test the effects of different cutoffs in cell type enrichment, we perform the same analysis as B and C while fixing the radius and steepness. We see the power of correctly assigned cell type marker back to its corresponding cell type has decreased at 0.5 cutoff, while little difference is seen at 0.75 and 0.85. We chose 0.75 cutoff for both mouse and human. The consistent result using different parameters shows the robustness of the method.